Dalton Transactions

ROYAL SOCIETY OF CHEMISTRY

PAPER

View Article Online
View Journal | View Issue

Cite this: *Dalton Trans.*, 2025, **54**, 3188

Reversible phase transition and tunable band gap in zinc telluride induced by acoustic shock exposure

Oviya Sekar,[a] F. Irine Maria Bincy,[a] Raju Suresh Kumar,[b] Kannappan Perumal,[a] Ikhyun Kim *[c] and S. A. Martin Britto Dhas *[a,c]

In this study, Zinc Telluride (ZnTe) was subjected to acoustic shock waves with a Mach number of 1.5, transient pressure of 0.59 MPa, and a temperature of 520 K to analyze its stability against shock wave impact. ZnTe was exposed to different shock pulses, such as 100, 200, 300, and 400. The stability was assessed through multiple characterization techniques such as Powder X-ray diffraction (PXRD), Raman spectroscopy, Ultraviolet diffuse reflectance spectroscopy (UV-DRS) analysis, Photoluminescence (PL) spectroscopy, and Scanning Electron Microscopy (SEM). The X-ray diffraction pattern revealed a phase transition at 300 shock pulses from cubic ($F\bar{4}3m$) to cubic ($Fm\bar{3}m$). Interestingly, at 400 shock pulses, the original cubic ($F\bar{4}3m$) phase was restored. The Raman spectrum showed the disappearance, intensity variation, and shift of Raman peaks, particularly at 300 shock pulses, which reverted to the original state at 400 pulses, indicating a reversible phase transition. The absorption spectrum exhibited a lower angle shift and a change in band gap from 2.85 eV to 2.63 eV at 300 shock pulses. However, the band gap was reduced to 2.8 eV at 400 shock pulses. The photoluminescence spectrum showed high intensity specifically at 300 shock-loaded conditions. Morphological analysis revealed a change from irregular shapes to plate-like structures at 300 shock pulses. The results confirm that shock waves significantly impact ZnTe, inducing a reversible phase transition.

Received 6th December 2024,
Accepted 6th January 2025

DOI: 10.1039/d4dt03393k

rsc.li/dalton

Introduction

Shock wave loading has emerged as an effective technique for modifying the characteristics of various materials, including crystalline, non-crystalline, and nanocrystalline forms. By rapidly compressing materials through controlled temperature and transient pressure adjustments, it is possible to induce substantial changes in their properties. The extreme levels of pressure, stress, tension, and temperature applied during shock wave loading can significantly alter material characteristics. Traditionally, static high-pressure compression and decompression methods have been used in high-pressure experiments, leading to the discovery of numerous reversible phase transition materials. Recently, significant advancements in dynamic shock wave techniques, particularly those produced by table top shock tubes, have revealed crystallographic phase transitions in materials critical for technology. These investigations have yielded fascinating discoveries in both bulk and nanoscale forms.[1–5] Due to their remarkable functional qualities, there is growing interest in molecular and crystallographic switchable dielectric, optical, and magnetic materials in the electronics industry. These materials are essential for developing devices used in data transmission, memory storage, signal processing, environmental monitoring, pressure transmitters, and sensor applications. Consequently, many laboratories actively search for highly efficient switchable phase transition materials, encompassing both bulk and nanoscale forms of inorganic and organic compounds.[6–8]

Materials capable of rapidly transitioning between two states hold great potential for next-generation applications, enabling frequent and fast switching. For example, recent studies have demonstrated that by altering the number of shock pulses, crystallographic switchable phase transitions can be induced in a bulk single crystal of potassium sulfate (K_2SO_4) that has β to α and α to β phases.[9] Similarly, nanoparticles such as Fe_2O_3 exhibit a crystallographic and molecular phase transition between α-Fe_2O_3 (hematite) and Fe_3O_4 (magnetite) under shock conditions,[10] Bi_2Te_3 exhibits a crystallographic reversible phase transition.[11] Moreover, numerous magnetically switchable phase transitions have been documen-

[a]*Shock Wave Research Laboratory, Department of Physics, Abdul Kalam Research Centre, Sacred Heart College, Tirupattur, affiliated to Thiruvalluvar University, Serkkadu, Tamil Nadu, 635 601, India. E-mail: martinbritto@shctpt.edu*
[b]*Department of Chemistry, College of Science, King Saud University, P.O. Box 2455, Riyadh 11451, Saudi Arabia*
[c]*Department of Mechanical Engineering, Keimyung University, Daegu 42601, Republic of Korea. E-mail: kimih@kmu.ac.kr*

ted in nanocrystalline materials of industrial importance, including $ZnFe_2O_4$ nanoparticles,[12] α-MnO_2,[13] Fe_2O_3,[10] and Co_3O_4.[14]

ZnTe, a well-known II–VI semiconductor, is highly regarded for optoelectronic applications due to its wide band gap. Its crystal structure is primarily cubic zinc blende (ZB), as indicated by its phase diagram. ZnTe's distinctive electrical and optical qualities make it particularly suitable for high-efficiency light-emitting diodes (LEDs) and laser diodes operating in the green region of the visible spectrum. This ability to emit light efficiently in this wavelength range makes ZnTe ideal for display technologies and laser-based devices.[15–17] Additionally, ZnTe is used in X-ray detectors, where its characteristics enable efficient X-ray detection, making it valuable for industrial inspection and medical imaging. Furthermore, ZnTe finds applications in solar cells, as its electrical properties can enhance energy conversion efficiency. It is also employed as a component of light-emitting devices or optoelectronic systems in television projectors, owing to its ability to produce bright and clear images. Moreover, ZnTe plays a crucial role in signal transmission technologies, utilizing its optical properties to improve communication systems. Its wide range of applications underscores ZnTe's significance in modern electronic and optoelectronic devices.[18–22]

Despite its potential, Zinc Telluride is relatively less studied at high pressure due to the research focus on other chalcogenide materials whose properties at high pressure have been investigated.[23] Early high-pressure experiments and theoretical studies on ZnTe have yielded several interesting results. For instance, ZnTe transitions to a non-metallic hexagonal phase (ZnTe-II) at 8.5 GPa and subsequently to a metallic phase (ZnTe-III) at 13 GPa, as demonstrated by a combination of XRD and electric resistivity measurements.[24] Nelmes *et al.* determined that the orthorhombic structure with *Cmcm* symmetry (B33) in the ZnTe-III phase is stable at 11.5 GPa and confirmed that the cinnabar structure emerges at a transition pressure of 8.9 GPa for ZnTe-II.[25–27] At high pressures of 12 to 85 GPa, ZnTe transforms from a cubic phase ($F\bar{4}3m$) to a cinnabar phase ($P3_121$) and then to an orthorhombic phase (*Cmcm*), accompanied by an electronic phase transition from semiconductor to metal. Under hydrostatic conditions, ZnTe undergoes two phase transitions: from the zinc blende phase to the cinnabar phase at 7–9 GPa, and then to the Cmcm phase at 11–13 GPa. Also, ZnSe undergoes phase transitions under pressure, shifting from zinc blende to cinnabar at ~4.9 GPa, followed by metallization at ~12.5 GPa. The transition pressure is delayed under hydrostatic conditions, and the phase change is irreversible under non-hydrostatic conditions due to constrained interlayer interactions.[28,29] Specifically, at 9.6 GPa, the initial zinc blende (ZB, ZnTe-I) structure transitions to a cinnabar phase (ZnTe-II), and at 12.1 GPa, a high-pressure orthorhombic phase (ZnTe-III) with Cmcm symmetry emerges. Kusaba *et al.* reported a space group $P3_1$ rather than $P3_121$ at 11.5 GPa pressure for ZnTe-II.[30]

To further investigate Zinc Telluride (ZnTe) under dynamic shock wave loading, it is crucial to expand on the findings from static high-pressure investigations. Dynamic shock waves can induce rapid and extreme pressure changes that might reveal additional phase transitions or modifications in ZnTe's properties that are not analyzed by static methods. The shock wave technique, with its ability to apply transient and high-pressure conditions, offers a unique opportunity to explore the behavior of ZnTe beyond the limitations of traditional static high-pressure experiments which often lack real-time observation and are constrained by slower pressure application rates. By subjecting ZnTe to controlled shock waves, researchers can probe the material's response in real time, potentially uncovering new phases or transitions that could impact its optoelectronic properties. Such experiments could provide valuable information on the stability and reversibility of different phases, including the potential for discovering novel phases or transitions between known phases. Furthermore, dynamic shock wave experiments could help elucidate the mechanisms behind ZnTe's electronic and structural transformations, offering deeper insights into its potential applications in advanced electronic and optoelectronic devices. This approach not only extends the fundamental understanding of ZnTe's behavior under extreme conditions but also paves the way for optimizing its performance in practical applications.

Experimental procedure & characterization techniques

In the current experiment, Zinc Telluride is purchased from Sigma Aldrich with a purity of 99.9% and then the sample was split into equal amounts and made into a small pouch, it was subjected to varying numbers of shock pulses, specifically as 100, 200, 300, and 400 pulses each with a Mach number of 1.5, transient pressure of 0.59 MPa, and temperature of 520 K. This is conducted using a semi-automatic Reddy tube (Yelagiri Technologies, model number ST2024YT02), as depicted in Fig. 1. The semi-automatic Reddy tube comprises three sections: the driver section, the driven section, and the diaphragm section. When the pressure reaches a critical level, the diaphragm ruptures, generating shock waves. These shock waves then propagate through the driven section toward the sample, secured in a sample holder. The transient pressure of 0.59 MPa for each shock pulse was measured using piezoelectric PCB transducers (Model 113B26) with a sensitivity of 1.465 mV kPa^{-1} and a linearity error of 1%. Calibration of the transducers was performed under identical high-temperature (520 K) and high-pressure conditions to ensure accuracy. The calibration process involved verifying the transducer response against a standard reference, with the standard error consistently remaining below 5%. This ensured high reliability and repeatability of the transient pressure measurements, providing a precise baseline for analyzing the effects of shock pulses on the samples. To further reduce measurement disturbances and eliminate unexpected impurities, the sample holder and the driver tube were cleaned after every other experiment.

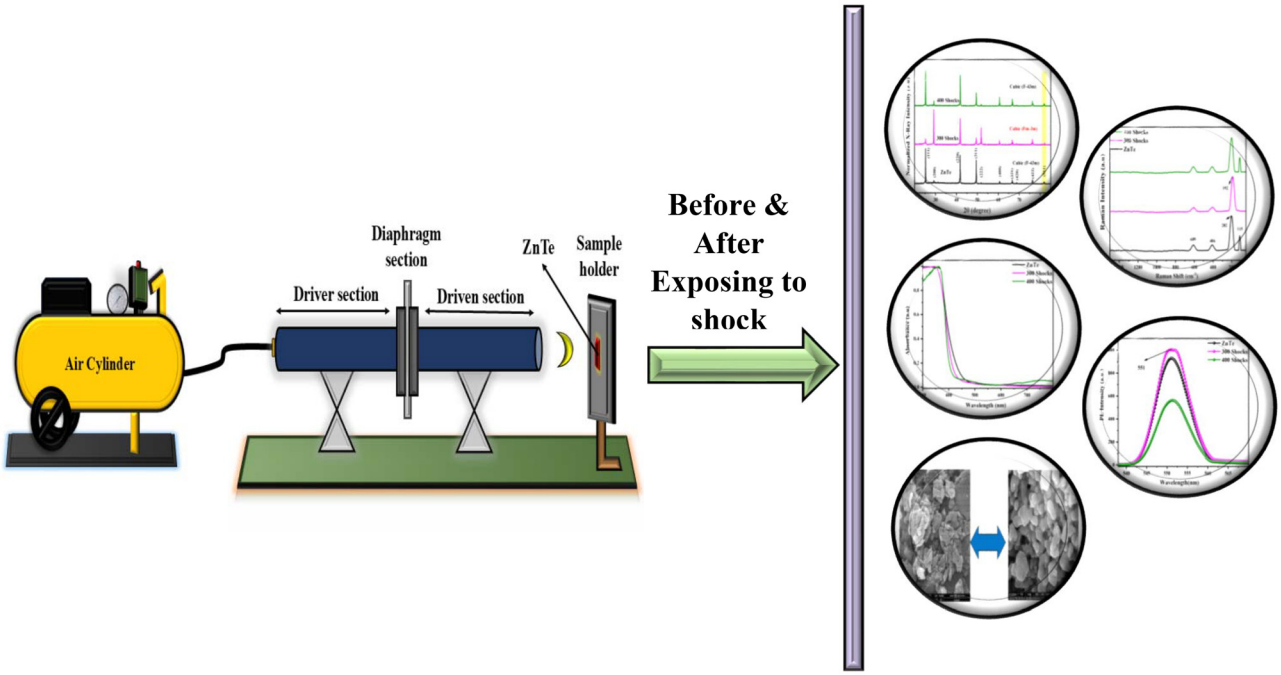

Fig. 1 Schematic representation of shock-loading experiment on ZnTe.

Once the samples have been subjected to the shock pulses, they are examined using various characterization techniques. The results from these shock-treated samples are compared with those from untreated samples to assess the effects of the shock waves. This comparison is essential for analyzing the stability of Zinc Telluride when exposed to shock waves and understanding its resilience against such impacts. The X-ray diffraction pattern of the sample was analyzed by using the instrument Brucker AXS D2 phaser, Cu Kα as a source with 1.5406 Å wavelength between the 2θ range of 20 to 85°. The Raman analyses were analyzed by using a confocal micro-Raman Spectrometer (LabRAM HR 800, Horiba Jobin Yvon Evolution model, He–Ne/325 nm laser used as a source), with results recorded between 100–1500 cm^{-1} with an excitation wavelength of 532 nm. The Ultraviolet diffuse reflectance spectroscopy (UV-DRS) analyses were recorded between 300–800 nm using JASCO Spectrometer. The morphology of the samples was analyzed by Scanning Electron Microscope (SEM) using the instrument TESCAN VEGA3 XMU with a resolution of 3.0 nm at 30 kV. The emission spectrum of the sample was recorded between 500 to 570 nm by using a PerkinElmer model LS 45 at the excitation wavelength of 325 nm.

Results and discussion

Powder X-ray diffraction analysis

The X-ray diffraction pattern of shock-untreated and treated ZnTe is shown in Fig. 2(b), the shock-untreated sample given in Fig. 2(a) shows peaks on the 2θ values of 25.31°, 29.31°, 41.93°, 49.61°, 51.85°, 60.79°, 66.93°, 68.91°, 76.59°, and 82.19° which are indexed with their corresponding *hkl* values as (111), (200), (220), (311), (222), (400), (331), (420), (422), and (511), respectively which is well matched with the standard JCPDS card number: 65-0385, which has a cubic structure with space group of $F\bar{4}3m$. The lattice parameters of ZnTe in this phase are $a = b = c = 6.114 \pm 0.002$ Å, also since it is a cubic structure $\alpha = \beta = \gamma = 90°$. The space group $F\bar{4}3m$ (216) means that f stands for the face-centered cubic lattice, and 43 m indicates the point group symmetry, which has 4-fold rotational symmetry axis, 3-fold rotational symmetry axis, and mirror planes corresponding to the zinc blende type materials. Ionic and covalent bonds hold the structure together with weak van der Waals force. The atomic arrangements in this structure are tetrahedral coordination where the Zn atom is surrounded by four Te atoms in a tetrahedral geometry[31,32] as shown in Fig. 2(c).

When this ZnTe is subjected to 100 shock pulses planes (111), and (200) show a reduction in the intensity, also plane (200) shows a slight split in the peak (like a shoulder peak), the plane (511) shows sharp intensity, at 200 shock pulses the peak (111), (200) remains in the same intensity, the plane (200) remains unchanged, plane (500) shows a slight drop in the intensity, the above-said planes are shown in their zoomed version in Fig. 3(a), (c), (d), and (e) though these changes have occurred the phase of the 100, 200 shocks remains unchanged. When the shock pulses are increased to 300 the plane (111) shows a further decrease in the intensity, but the plane (200) in Fig. 3(b) shows a drastic and remarkable increase in their intensity, plane (200) shows a slight converging of shoulder peak, and also, plane (222) in Fig. 3(d) shows an increase in their intensity, remarkably plane (511) shows a shift towards a

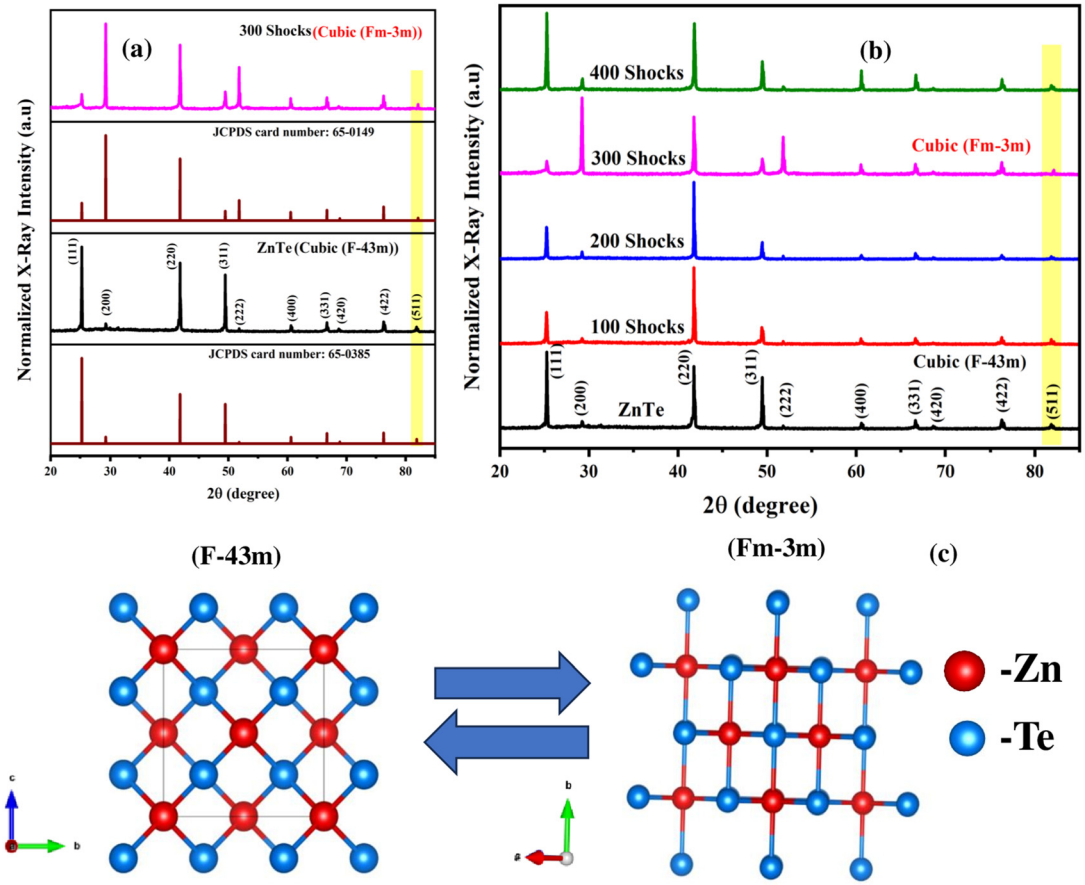

Fig. 2 X-ray diffraction pattern of ZnTe (a) standard pattern of ZnTe (b) diffraction pattern of shock-untreated and treated ZnTe (c) structure of cubic ($F\bar{4}3m$) and Cubic ($Fm\bar{3}m$).

higher angle, these changes make more concern about the sample at this particular shock pulses. Since there is a slight decrease in the unit cell volume at 100, 200 shock pulses as shown in the Table 1 which shows that lattice compression is occurred these also might be a reason for the variation of intensity.

Also, the XRD pattern of 300 shock loaded sample shows a different pattern compared to the 100, and 200 shock pulses, since there is a drastic change in their intensity, also as a shift in the peak, which makes it more interesting to analyze the effect of shock pulses. Surprisingly the XRD pattern obtained in the 300 shock pulses which is well fitted with the standard JCPDS pattern card number: 65-0149, even the shifted peak also belongs to the same card number, also shows a same intensity variation just similarly obtained to 300 shocked samples shown in Fig. 2(a). The shifted peak is highlighted in Fig. 2(b) and the zoomed-in version is shown in Fig. 3 (e). More interestingly the peak matched with the standard pattern shows the same cubic structure with different space groups $Fm\bar{3}m$, also incredibly the pattern has the same *hkl* values as for the space group $Fm\bar{3}m$ as, (111), (200), (220), (311), (222), (400), (331), (420), (422), and (511), the only key difference between the unshocked, 100 and 200 shock pulses is the intensity variation, shift in the peak, space group, also a slight variation in their structure, the structure of the space group $Fm\bar{3}m$ is shown in Fig. 2c.

The space group $Fm\bar{3}m$ (255) means that F stands for the face-centered cubic lattice, and $m\bar{3}m$ indicates the point group symmetry with mirror planes and 3-fold rotation corresponding to the Zinc blende or sphalerite structure. In this structure, each Zn atom is tetrahedrally coordinated with four Te atoms, and each Te atom is similarly coordinated with four Zn atoms. The structure is held together by ionic and covalent bonds with electrostatic forces.[33,34] Therefore, it is confirmed that at 300 shock pulses the material has undergone a phase change from cubic ($F\bar{4}3m$) to cubic ($Fm\bar{3}m$). There is a decrease in the unit cell volume shown in Table 1 which shows that the sample completely causes compression in their lattice, also the value of lattice parameters of axes *a*, *b*, and *c* shows a decrease in value, making the bonds to compress and change the atomic position, this induces the phase transition in the sample.

When shock pulses of 400 are increased the material shows the changes in the intensity and shift of the peak. As said in the above passage the changes in the plane (111), (200), (220), (222), (511) shown in Fig. 3(a)–(e) all retain their originality just like the shock untreated sample. Plane (111) shows a sharp intensity, (200), and (222) planes show a drastic drop in

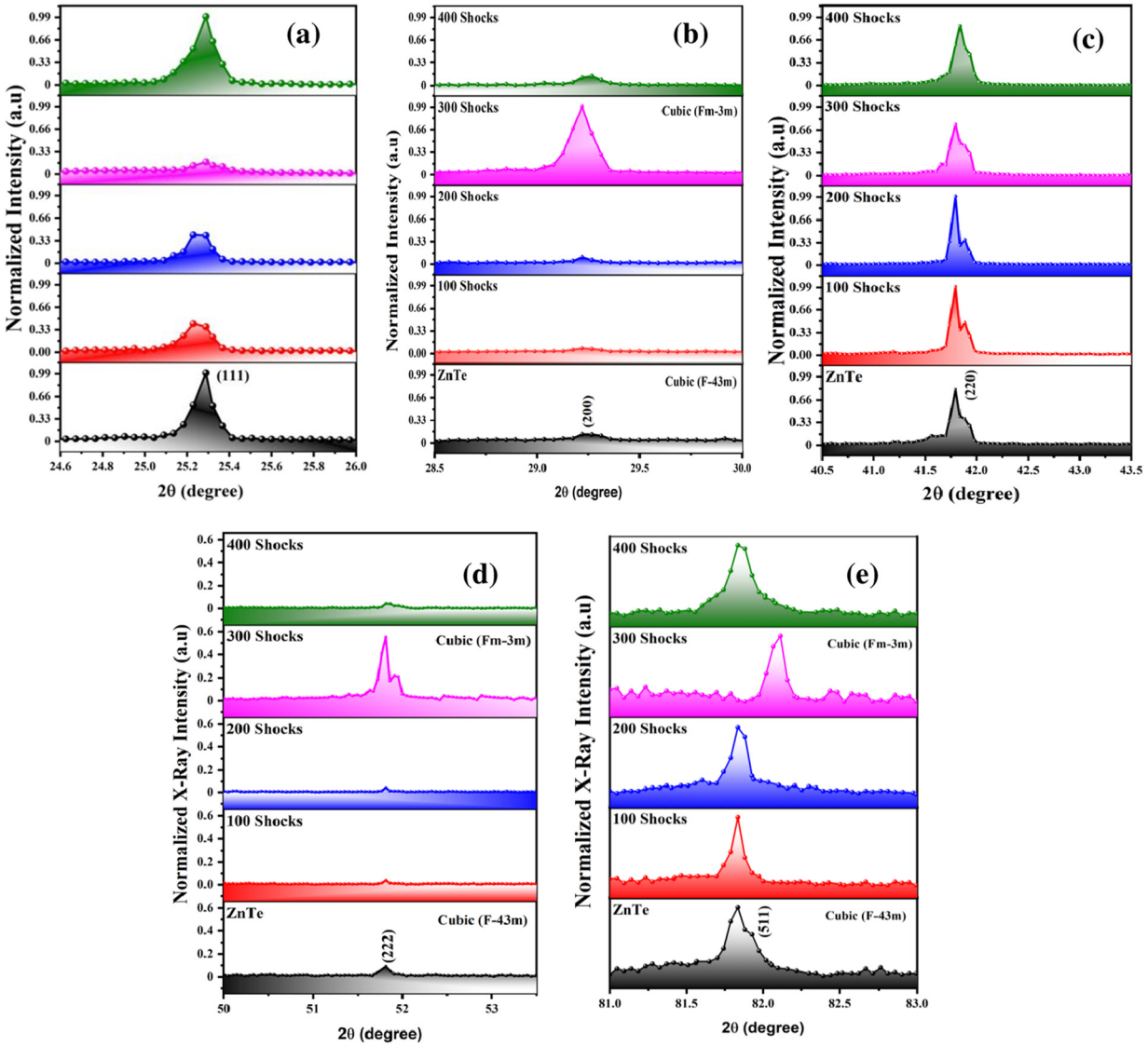

Fig. 3 Zoomed in XRD pattern of shock-untreated and treated ZnTe (a) between 24.6° to 26.0° (b) between 28.5° to 30.0° (c) between 40.5° to 43.5° (d) between 50° to 54° (e) between 81° to 83°.

Table 1 Refinement parameters of shock-untreated and treated ZnTe

Samples	ZnTe	100 shocks	200 shocks	300 shocks	400 shocks
Crystal system	Cubic	Cubic	Cubic	Cubic	Cubic
Space group	$F\bar{4}3m$	$F\bar{4}3m$	$F\bar{4}3m$	$Fm\bar{3}m$	$F\bar{4}3m$
Lattice parameters					
$a = b =$ c	6.114 ± 0.002	6.113 ± 0.002	6.112 ± 0.002	6.07 ± 0.002	6.115 ± 0.002
$\alpha = \beta = \gamma$	90	90	90	90	90
Unit cell volume	228.34 ± 0.05	228.32 ± 0.05	228.28 ± 0.05	225.76 ± 0.05	228.51 ± 0.05
GOF	1.80	1.86	1.81	1.80	1.79

intensity, plane (220) shows the convergence of shoulder peak, also (511) plane shifted again to its original position and moved towards lower angle, and the obtained pattern which matches with same standard pattern JCPDS card number: 65-0385, all the changes obtained in the 400 shock pulses are well figured in Fig. 3(a)–(e). This shows that shock waves have the capability of phase transition and also reverse the phase. The reversible phase change of the material is caused due to the lattice expansion, it is evident from the refinement parameters such as lattice parameters, and unit cell volume of the sample

shows an increased and reversed condition similar to shock-untreated, 100, and 200 shocks. This shows that the lattice expansion causes the bonds to expand more and makes the atoms misplace to their original place, which induces reversible phase transition.

Generally, when subjected to shock pulses, materials experience a sudden, intense stress that can induce rapid deformation of the crystal lattice. This deformation may manifest as either lattice relaxation or expansion, influenced by the material's intrinsic structural properties and response to the applied stress.[35,36] Lattice relaxation can occur as atoms shift slightly within the crystal framework, absorbing some of the energy and potentially reducing internal strain. Conversely, lattice expansion may take place if the shock waves force atoms apart, increasing the volume within the crystal structure temporarily.[37] As the shock impact propagates through the lattice, a uniform tensile strain frequently develops perpendicular to the direction of wave propagation. This strain distorts the lattice, increasing interplanar spacing (*d*-spacing), which may result in a noticeable shift of diffraction lines in X-ray diffraction (XRD) patterns. Typically, such strain shifts diffraction peaks to lower angles due to increased *d*-spacing, but in specific scenarios, structural adjustments could cause peak shifts to higher angles.[37] The rapid compression introduced by shock waves also significantly affects diffraction peak intensities.

This compression can promote dynamic recrystallization, where atoms in the lattice attempt to rearrange into more stable configurations to mitigate the high-energy state induced by the shock. However, the transient nature of the shock waves persisting only for a brief period, means that the system is under constant kinetic and thermal constraints. However, under rapid, transient shock conditions, there may not be sufficient time for atoms to fully stabilize at lower energy levels immediately after the shock wave dissipates. This fleeting stability can result in temporary or reversible phase changes, as observed with the transitions from $F\bar{4}3m$ to $Fm\bar{3}m$ and back to $F\bar{4}3m$. These rapid changes manifest in XRD data as shifts, peak broadening, or intensity fluctuations, reflecting the adaptive behavior of the crystal structure under high-pressure, short-duration conditions.[35,36]

In the Fig. 4, we proposed a mechanism of phase transition in zinc telluride (ZnTe) induced by shock compression and expansion. ZnTe initially occurs in a cubic phase with the space group $F\bar{4}3m$ (shown in Fig. 4(a)), which remains stable under low-to-moderate shock pulses, specifically for 100, and 200. This $F\bar{4}3m$ structure is characterized by a precise arrangement of zinc (Zn) and tellurium (Te) atoms with set bond angles and lengths that ensure structural stability without severe lattice distortion. ZnTe experiences a phase change to a cubic structure with the $Fm\bar{3}m$ space group when exposed to a higher number of shocks, specifically, 300 shock pulses, as seen in Fig. 4(b)

The lattice compression brought on by the shock-induced high-pressure environment is responsible for this phase shift. The Zn and Te atoms are forced closer together by extreme compression, changing the atomic structure and creating new Zn–Te bonds. As atoms move to reduce internal strain, these extra bonds aid in stabilizing the crystal lattice under elevated pressure. The increased electrostatic forces between Zn and Te atoms, which are kept at closer distances and have larger interaction energies, produce a more compact, isotropic structure in the $Fm\bar{3}m$ phase. The compression of the sample is well identified using the refinement of the XRD pattern, which shows that slight decrease in unit cell volume from 228.34 $Å^3$ to 225.67 $Å^3$, as shown in Table 1 and their corresponding variation plot is shown in Fig. 6(c) which confirms that lattice compression has taken place in the sample.

When the shock strength is increased to 400 pulses, the sample shows a reversed condition *i.e.*, ZnTe reverts to its initial $F\bar{4}3m$ phase at this elevated shock level. At this higher pressure, the extra bonds created during the transition to the

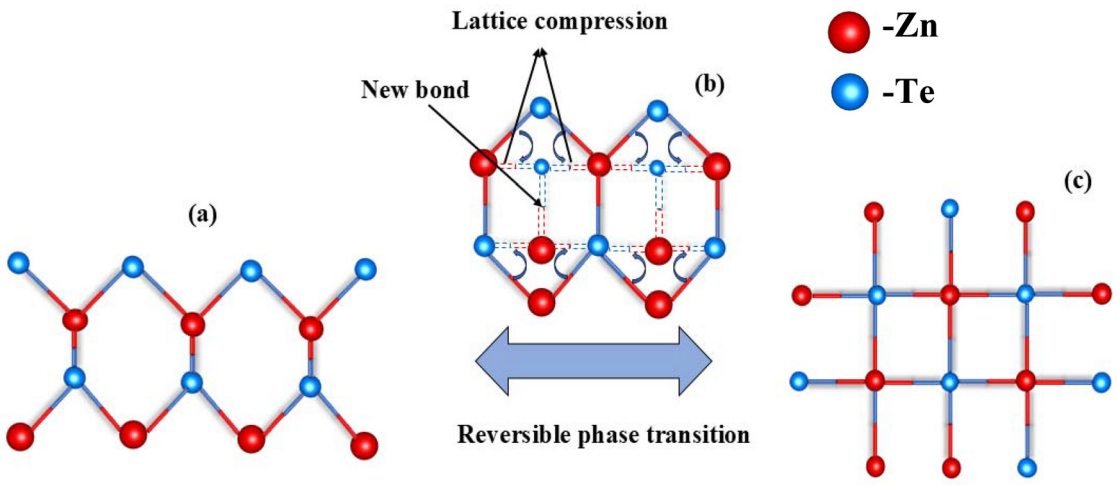

Fig. 4 Proposed mechanism of phase transition and reversible in ZnTe (a) Structure of cubic ($F\bar{4}3m$) of shock-untreated, 100, 200, and 400 shocks (b) proposed reversible phase change by the formation of new bond and lattice compression (c) Structure of Cubic ($Fm\bar{3}m$) of 300 shocks

$Fm\bar{3}m$ phase become unstable due to the rapid release of energy inherent to the shock wave environment. The dynamic shock conditions involve brief, intense pressure and temperature spikes, followed by equally rapid decompression. This transient high-pressure state can cause temporary bond rearrangements to stabilize the structure momentarily. However, as the shock dissipates, the thermodynamic stability of the original $F\bar{4}3m$ phase reasserts itself. The crystal reverts to its original configuration because the energy landscape favors the lower-energy arrangement of the $F\bar{4}3m$ phase under ambient conditions. This behavior suggests that the material undergoes a phase change under high pressure but reverts to its original structure afterward. The newly formed phase becomes unstable as the energy dissipates, and the original $F\bar{4}3m$ phase reasserts itself due to its thermodynamic favourability.

This reversion highlights the material's inherent resilience and preference for the lower-energy configuration, which prevents the sustained presence of the high-pressure phase. This reversion implies that the structural alterations brought about by the 300 pulses are transient and can be reversed by more shock-loading as opposed to only decompression. The decompression of the sample is confirmed by the refinement parameters shown in Table 1, the unit cell volume of the sample increased from 225.67 $Å^3$ to 228.58 $Å^3$ as shown in Fig. 6(c), more or less similar to shock-untreated, which shows that the lattice expansion can induce the phase change of the material. Therefore, the proposed mechanism shows that due to lattice compression and expansion, there is shrink and expansion in the bonds, and a new bond formed connects the interchanged atoms during this process induces phase change and also, reversible phase change in the material. ZnTe's resilience is demonstrated by this reversible phase transition, which highlights its potential for applications needing materials that can withstand and adapt to harsh conditions by alternating between different structural configurations according on the applied shock pulses.

For further confirmation of the reversible phase transition the Rietveld refinement analysis was carried out using the Full Prof-Suite software, and their corresponding plots are shown in Fig. 5, the refinement parameters are derived by utilizing the pseudo Voigt function, corresponding refinement parameters are shown in Table 1, though there is a variation in the intensity of some planes in the 100, and 200 shocks the peaks are well fitted in the same cubic ($F\bar{4}3m$) space group, which shows the stability of the sample in minimal pressure, also the parameters like a, b, c and unit cell volume shows a reduction in their values shows a slight compression is started in the sample, at 300 shock pulses the dramatic changes where caused due to high pressure and temperature, which is also well fitted in the cubic phase of space group ($Fm\bar{3}m$), with a goodness of fit 1.80, along with little reduction of lattice parameters and unit cell volume as 6.07 Å, 225.76 $Å^3$, respectively. The well-fitted refined plot confirms the phase change of the sample, when shock pulses of 400 are applied the phase retains the original phase which is also well in agreement with

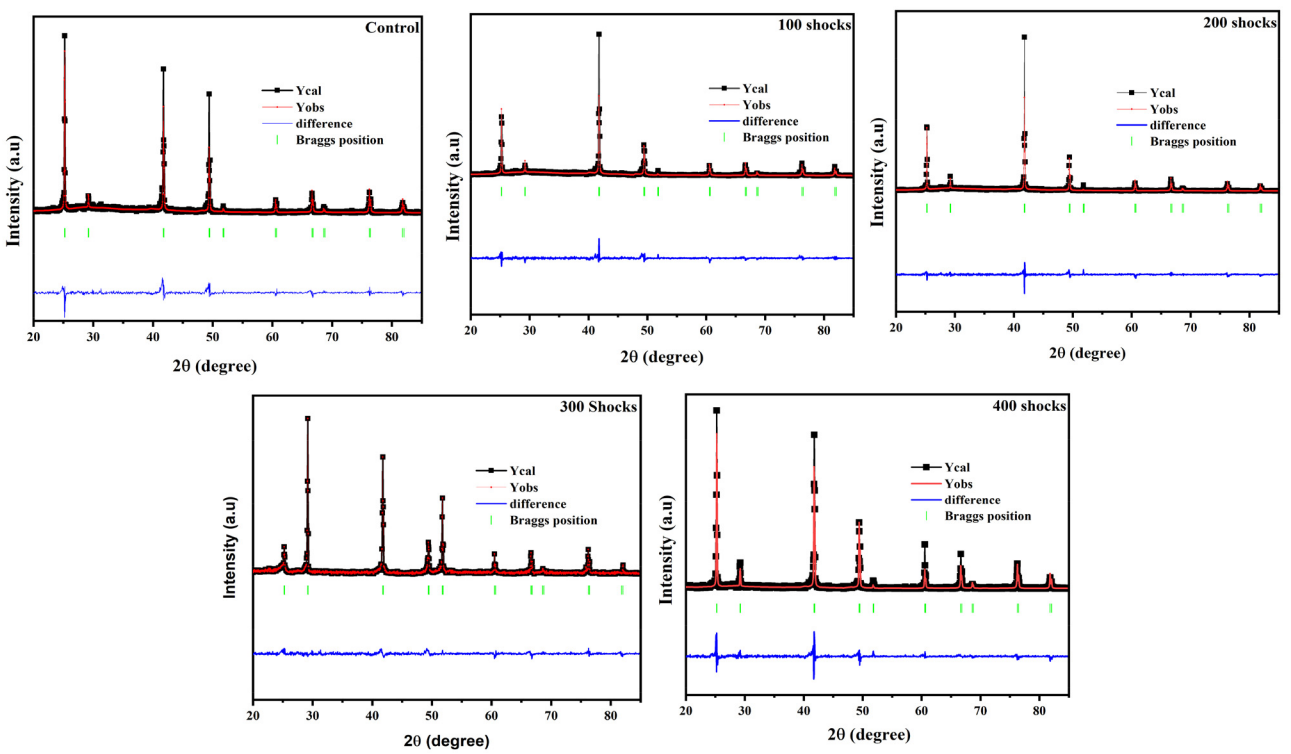

Fig. 5 Refinement plots of shock-untreated and treated ZnTe.

the phase cubic ($F\bar{4}3m$), also their lattice parameters show a similarity of unshocked conditions. Therefore, shock-induced reversible phase transition is well proved from the refinement data and plots. The corresponding variation plots of lattice parameters are well figured in Fig. 6(c) and (d)

The dislocation density and lattice strain of ZnTe provide insights into the material's structural evolution under shock wave exposure. Dislocation density (δ) measures the concentration of defects within the crystal lattice and was calculated using the equation $\delta = 1/D^2$ where D represents the crystallite size. This crystallite size was obtained through the Debye–Scherrer formula, expressed as $D = K\lambda/\beta\cos\theta$. Here, K is a dimensionless shape factor, λ is the X-ray wavelength, β is the full width at half maximum (FWHM) of the diffraction peak, and θ is the Bragg angle. Lattice strain $\varepsilon = \beta/4\tan\theta$, capturing the degree of distortion in the crystal structure due to defects.

Fig. 6(a) and (b) display the relationships between crystallite size, dislocation density, and lattice strain of shock-treated and untreated ZnTe. Initially, for the untreated ZnTe, the average crystallite size was 26.56 nm. Upon applying shock pulses, a systematic fluctuation in crystallite size was observed. After 100 shock pulses, the crystallite size increased to 28.01 nm, suggesting a reduction in internal stresses, leading to the growth of crystal domains. After 200 shock pulses, the crystallite size slightly increased to 30.08 nm, followed by a greater increase to 32.81 nm after 300 pulses. With further shock exposure, the crystallite size decreased to 27.89 nm at 400 pulses, indicating a similarity of the unshocked sample. The increase and decrease in crystallite size correspond to a fluctuation in FWHM values, dislocation density, and lattice strain, signalling improvements in ZnTe's crystallinity at initial shock-loading samples. As crystallite size grows, dislocation density decreases due to the merging of grain boundaries or elimination of crystal defects.[38] The lattice strain also diminishes, reflecting a relaxation of internal stresses and a decrease in lattice imperfections. This trend suggests that shock pulses act as a form of annealing, reducing defects and enhancing crystalline order by allowing atoms to settle into more stable positions within the lattice. The result is sharper X-ray diffraction peaks, which correspond to a more ordered, defect-free crystal structure.[39] The observed changes in XRD peak intensities and shifts can be attributed to variations in crystallite size. As the grain size increases due to initial shock pulses, the dislocation density decreases, resulting in a reduction of internal stresses. This phenomenon directly impacts the lattice compression and expansion, influencing the peak positions and intensities. Such grain size-dependent effects on the crystal lattice further contribute to observable spectral variations, confirming the inter-

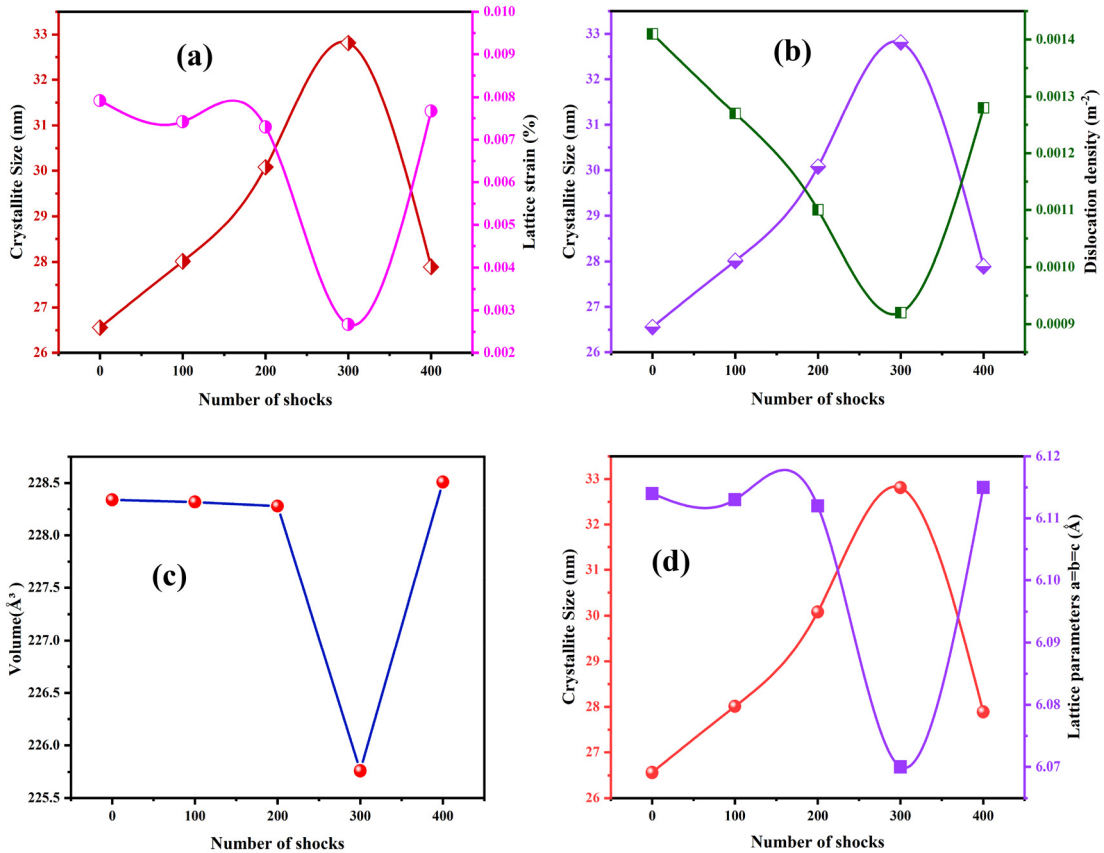

Fig. 6 Variation plots against the number of shock pulses (a) crystallite size *vs.* lattice strain (b) crystallite size *vs.* dislocation density (c) volume *vs.* the number of shocks (d) crystallite size *vs.* lattice parameters.

play between crystallite size and structural stability. Thus, with each increase in shock pulse count, the ZnTe structure undergoes a refining process, where imperfections and grain boundaries are gradually minimized at 300 shock pulses due to the phase transition, the material has undergone an increased trend in the dislocation, lattice strain. The variation in crystallite size and other parameters might be due to breakage and fusion of grain boundaries which is dynamic recrystallization.[40]

In summary, the XRD analysis demonstrates ZnTe's structural resilience and reversible phase transition behavior under shock loading. Initially stable up to 200 shocks, ZnTe undergoes a phase change at 300 shocks, shifting from $F\bar{4}3m$ to $Fm\bar{3}m$ symmetry. This new phase remains stable for months of time at ambient temperature after the shock waves have passed. However, upon further shock loading to 400 shocks, the structure reverts to the original $F\bar{4}3m$ phase. This behavior indicates that while ZnTe can undergo stable phase changes under stress, it tends to revert to its initial phase under higher levels of continued shock, showcasing its adaptability and resilience.

Williamson–Hall plot analysis

A useful tool for examining many microstructural characteristics in materials, including dislocation density, internal stress, lattice strain, and crystallite size, is the Williamson–Hall (W–H) plot. These factors all work together to affect changes in crystallite size. Using the broadening of X-ray diffraction (XRD) peaks to derive these characteristics, the W–H approach provides information about how mechanical treatments, such as shock waves, affect the material's structure. Fig. 7 presents the Williamson–Hall plot for Zinc Telluride (ZnTe) both shock wave treated and untreated whose value for the linear fit is 0.98, with $4\sin\theta$ plotted on the x-axis and $\beta_{hkl}\cos\theta$ on the y-axis. The crystallite size and microstrain values were derived from the slope of a linear fit to this plot, where the intercept reflects crystallite size, and the slope provides the microstrain. The crystallite size calculated *via* the W–H plot closely aligns with the values obtained using the Debye–Scherrer method, confirming consistency across these techniques. Additionally, Table 2 lists the calculated strain values, demonstrating that shock waves induce changes in crystallite size.

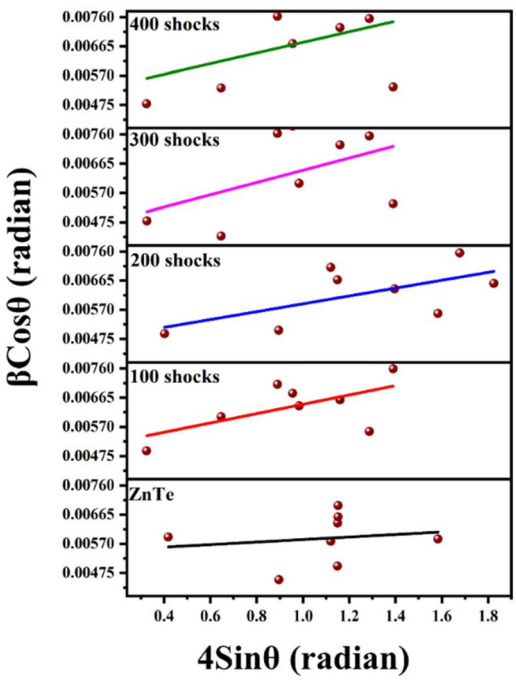

Fig. 7 W–H plots of shock-untreated and treated ZnTe.

Table 2 Calculated crystallite size of shock-untreated and shock-treated Zinc Telluride using Debye–Scherrer and W–H plot

Samples	Scherrer method, D (nm)	Williamson–Hall plot, D (nm)	Strain
0	26.56 ± 0.5	25.67 ± 0.4	0.0079 ± 0.0002
100	28.01 ± 0.6	28.29 ± 0.5	0.0074 ± 0.0002
200	30.08 ± 0.7	30.14 ± 0.6	0.0073 ± 0.0002
300	32.81 ± 0.8	31.51 ± 0.7	0.0026 ± 0.0002
400	27.89 ± 0.6	27.73 ± 0.5	0.0076 ± 0.0002

Vibrational analysis

Fig. 8 shows the Raman spectra of shock-untreated and treated ZnTe. The Raman spectrum of shock-untreated ZnTe reveals four key peaks, providing insights into the vibrational properties of the material. The peak observed at 115 cm^{-1} is attributed to Tellurium (Te) vibrations, possibly indicating the presence of elemental Te or Te-related modes within the ZnTe structure.[41] The peak around 202 cm^{-1} represents the first-order longitudinal optical (LO) phonon modes, which are characteristic of the intrinsic lattice vibrations of ZnTe.[42] Additionally, a weak peak at 406 cm^{-1} corresponds to the first overtone or second-order Raman mode, arising from the interaction of two phonons of 202 cm^{-1} each, indicative of non-

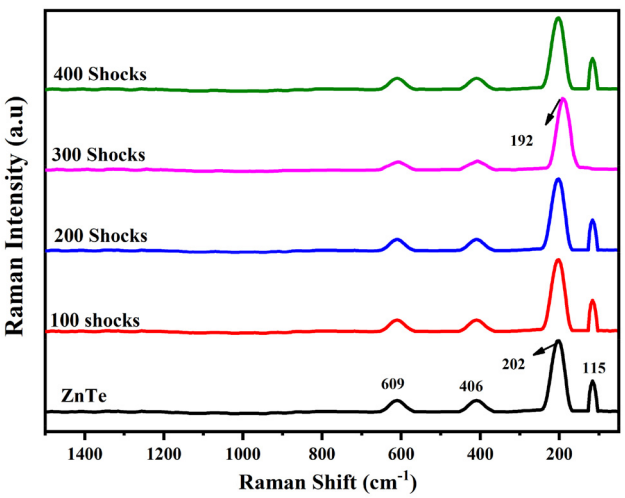

Fig. 8 Raman spectrum of shock-untreated and treated ZnTe between the range of 100–1500 cm^{-1}.

linear phonon interactions in the lattice.[42] The peak at 609 cm^{-1} is associated with the third-order longitudinal optical (3LO) phonon mode, resulting from the simultaneous excitation of three longitudinal optical phonons (each around 202 cm^{-1}).[43]

At 100 and 200 shock pulses, the Raman spectrum of ZnTe remains same, with no changes in peak positions, intensity, or spectral features. This consistency suggests that shock treatment at these levels has no effect on the ZnTe sample's crystal structure or phase composition. The stability of peak positions indicates that the lattice parameters are unchanged, implying that the crystal's fundamental structure has not been altered by the applied shocks. Similarly, the constant peak intensity indicates that there is no increase in crystallographic disorder or decrease in crystallinity; the arrangement of atoms within the lattice is preserved. Furthermore, the absence of peak shifts indicates that the material has not undergone changes in internal stress or pressure that could affect bond lengths or lattice symmetry. These findings suggest that shock exposure with 100 and 200 pulses is insufficient to induce phase transformation or significant structural changes in ZnTe. Thus, the material maintains its original phase stability and structural integrity while demonstrating a strong resistance to phase changes under moderate shock conditions.

At 300 shock pulses, the sample exhibits significant changes in its Raman peaks. Notably, the peak at 115 cm^{-1} has disappeared. Grain size variations also significantly influence the Raman spectral features. The disappearance and reappearance of the 115 cm^{-1} peak with increasing shock pulses are indicative of changes in lattice dynamics and phonon scattering mechanisms, which are inherently linked to grain size evolution and defect density. The observed shifts in vibrational modes correlate with the strain induced by grain size-dependent lattice compression and expansion. Analysis of the refinement parameters indicates that the unit cell volume for the shock-untreated and 100, 200 shock pulse samples was 228.33 $Å^3$. However, this volume decreased to 225.76 $Å^3$ after 300 shock pulses, suggesting that lattice compression has occurred in the sample. This compression likely leads to the disappearance of certain Raman modes, thereby confirming a structural transition.[44] The disappearance of the 115 cm^{-1} peaks given in Fig. 9(a) indicates a phase transition from cubic ($F\bar{4}3m$) to cubic ($Fm\bar{3}m$), consistent with observations reported in the previous literature.[44] Additionally, the peak at 202 cm^{-1} shifted to a lower wavenumber of 192 cm^{-1} as shown in Fig. 9(b). This peak is associated with the first-order longitudinal optical modes[45] and suggests that tensile strain has developed within the sample. Notably, this shift occurs after 300 shocks, but by 400 shocks, the peak reverts to its original position, indicating that the change is reversible. This behavior suggests that the shift is a transient effect induced by the shock waves, rather than a stable phase transition. The sample returns to its original phase after the shock-induced strain dissipates. Furthermore, the intensities of the peaks at 609 cm^{-1} and 406 cm^{-1} decreased in comparison to those in the shock-untreated and 100, and 200 shock pulse samples given in Fig. 9(c). Collectively, these observations confirm that a phase transition occurs specifically at 300 shock pulses. These findings are also supported by corresponding changes observed in the X-ray diffraction (XRD) patterns, reinforcing the conclusion that shock waves induce a transition from cubic ($F\bar{4}3m$) to cubic ($Fm\bar{3}m$) structures.

When shock pulses are increased to 400, the previously disappeared peak reappears, while the shifted peak returns to its original position at 202 cm^{-1}. Additionally, the intensity of this peak rises again shown in Fig. 9(a, b and c). The XRD

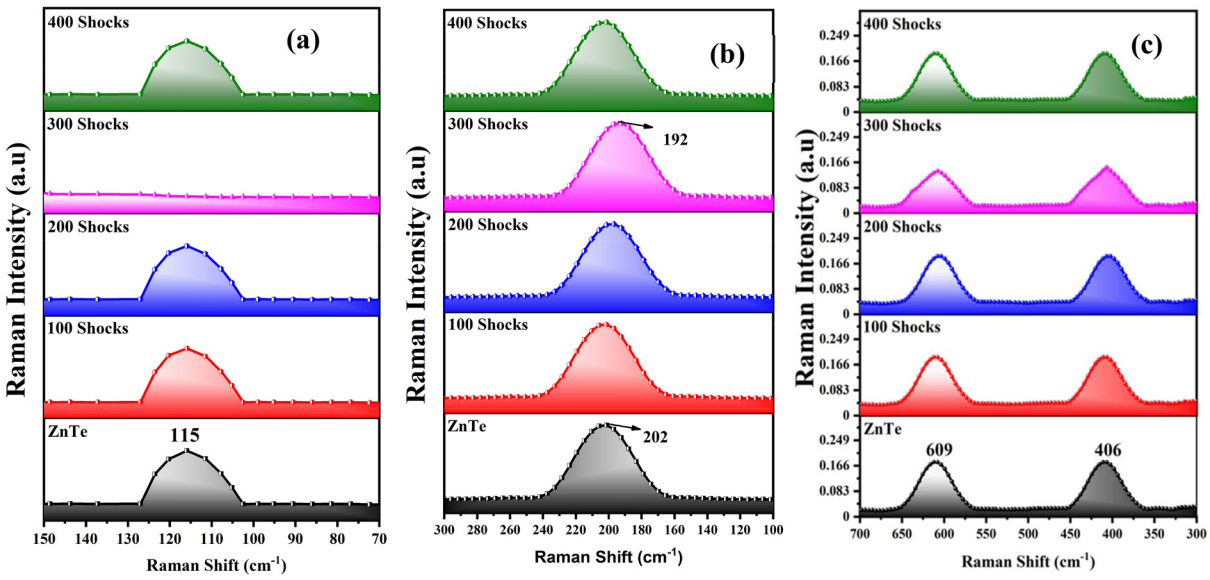

Fig. 9 Zoomed in Raman spectrum of shock-untreated and treated ZnTe (a) between the range of 150 to 70 cm^{-1}, (b) between the range of 300 to 100 cm^{-1}, (c) between the range of 700 to 300 cm^{-1}.

pattern also shows a transition from cubic ($F\bar{4}3m$) to cubic ($Fm\bar{3}m$), implying that the phase transition has reversed in the sample. Also, the sample volume increased to 228.33 Å^3 based on the refinement parameters. This confirms that lattice expansion occurred in the sample, resulting in peak shift and reappearance, as well as intensity increases under 400 shock conditions. This expansion is most likely caused by the increased energy input from the shock pulses, which aids in the restoration of the atomic structure and contributes to the appearance of peaks with higher intensities in the Raman spectrum. Based on the result of the XRD pattern and Raman analysis, it is confirmed that the phase transition is reversed. These findings underscore the dynamic nature of phase stability in ZnTe under varying shock conditions, offering insights into the material's response to high-pressure environments. Also, several factors may contribute to these phenomena, including defect healing, which removes structural imperfections caused by previous shock loading, allowing for a more stable configuration. Furthermore, localized heating caused by repeated shock waves may help overcome energy barriers for phase transitions, facilitating lattice recovery and improving phonon interactions.[46,47]

Ultraviolet diffuse reflectance spectroscopy analysis (UV-DRS)

The material's electronic spectra must be examined to assess the optical properties of shock-untreated and shock-treated zinc telluride (ZnTe) samples for use in photodetector and optoelectronic applications. A material's practicality for these applications is heavily influenced by its absorption spectrum, which provides information on how the material interacts with light at various wavelengths. A JASCO spectrometer was used to investigate ZnTe's optical absorption spectrum in the 300–800 nm range. Fig. 10(a) depicts the results, providing significant information on the material's absorption behavior and appropriateness for photodetectors and other optoelectronic devices. Before the exposure of shock waves, ZnTe shows an adsorption edge value of 433 nm. After exposure to shock waves like 100, 200, and 300 the adsorption edge shifted towards a higher wavenumber and constantly showed an increase in the adsorption edge value. Further, at 400 shock pulses, the adsorption edge shifted towards a lower wavenumber, those values are shown in the Table 3.

In the present study, shock pulses from 100 to 300 resulted in a pronounced shift towards higher wavenumbers, indicating progressive lattice compression. At 300 shock pulses, the material exhibits maximum compression, confirmed by a reduced band gap of 2.6 eV, signifying a phase change. The refinement parameters in Table 1 further substantiate this phase transformation: both lattice constants and unit cell volume decrease markedly, particularly at 300 pulses. This significant reduction in unit cell volume suggests a cubic ($F\bar{4}3m$) to cubic ($Fm\bar{3}m$) transition induced by the shock waves. However, with an increase to 400 shock pulses, the material appears to return to a state resembling the unshocked sample. Both the unit cell volume and lattice constants revert to their original values, indicating a reversible phase transition. This is corroborated by a shift of the absorption edge towards lower wavenumbers, comparable to that of the untreated sample, and by the observed band gap, which mirrors that of the unshocked state. These findings confirm that the phase change induced at 300 shocks is reversible upon further 400 shock loading.

The band gap of the material was calculated using a Tauc plot using the formula $(\alpha h\nu) = A(h\nu - E_g)^n$, and the corresponding figure is shown in Fig. 10(b), the band gap of the material is depicted in the Table 3 which is well consistent with previous literature.[48,49] This shows that from initial shock pulse 100 to 300 the band gap of the material is decreased, particularly at 300 shock pulses the band gap changed from 2.85 eV to 2.63 eV, which shows that the band gap of the material is tuned, which is due to the continues lattice compression, also the repeated shock waves cause to the appear-

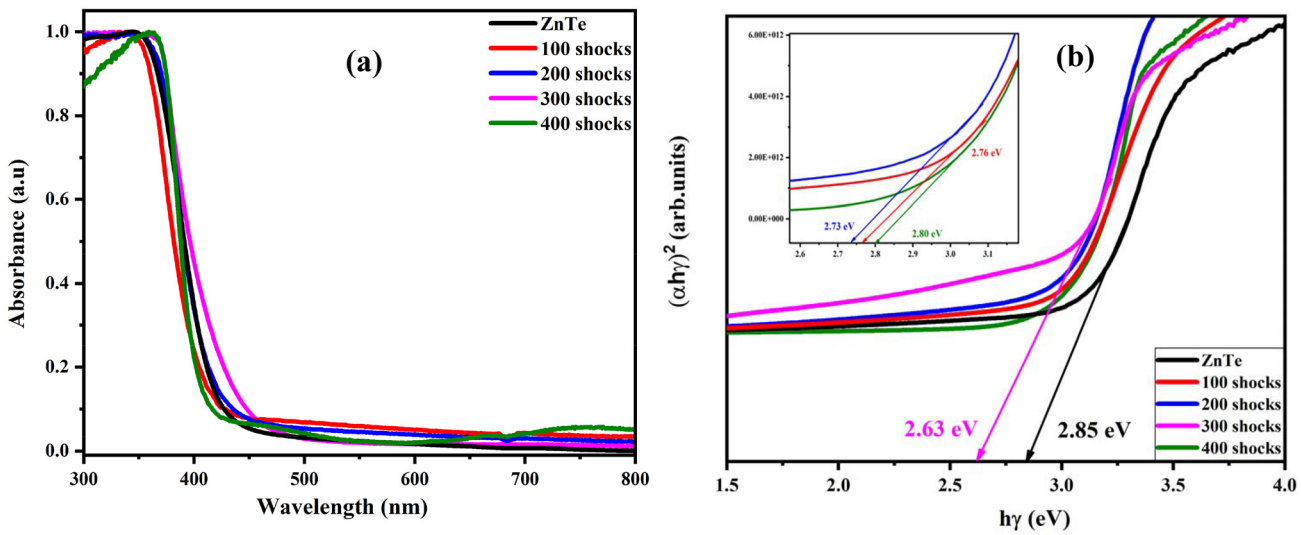

Fig. 10 (UV-DRS) analysis of shock-untreated and treated ZnTe (a) absorption spectrum of ZnTe, (b) Tauc plot of ZnTe.

Table 3 Value of adsorption edge, crystallite size, band gap against the number of shock pulses

No. of shocks	Adsorption edge (nm)	Crystallite size (nm)	Band gap (eV)
0	433 ± 2.5	26.56 ± 0.5	2.85 ± 0.05
100	444 ± 2.8	28.01 ± 0.6	2.76 ± 0.04
200	456 ± 3.0	30.08 ± 0.7	2.73 ± 0.04
300	467 ± 3.2	32.81 ± 0.8	2.63 ± 0.03
400	421 ± 2.6	27.89 ± 0.6	2.80 ± 0.05

ance of localized energy bands between the valence and conduction band, which is known as Urbach band. The observed variation in the band gap is in good agreement with the photoluminescence (PL) analysis, where the PL intensity increased up to 300 shocks, correlating with the band gap reduction, suggesting enhanced radiative recombination. However, after 400 shocks, the PL intensity decreased, aligning with the recovery of the band gap to its original value, indicating that the material's optical properties reverted to those similar to the unshocked state. The correlation between the lattice constant and band gap is well figured in Fig. 12(b). At 400 shock pulses again the band gap got reversed to 2.80 eV, also the lattice constant, and unit cell volume increased, this confirms that lattice expansion occurred due to the repeated shock pulses, also shock waves can induce the removal of localized energy bands between the valence and conduction band, due to the application of high pressure and temperature which leads to increase in the band gap.[50–53] The corresponding energy level diagram is shown in Fig. 11, the diagram shows the creation and annealing of Localized energy states *i.e.*, Urbanch tail due to the increased number of shock waves. The expansion and contraction of the ZnTe mechanism that induces band gap changes are well-figured in the proposed mechanism of Fig. 4

When subjected to shock pulses, the sample undergoes rapid compression, causing the crystal lattice to contract or expand, displacing atoms from their initial positions within the structure.[54] Lattice contraction brings atoms closer together, reducing both lattice parameters and atomic distances, which leads to increased overlap of electronic orbits. This enhanced overlap lowers the energy needed for electronic transitions, resulting in a smaller bandgap. Conversely, lattice expansion widens atomic separation, raising the bandgap.[55,56] Notably, after 400 shock pulses, the bandgap widened compared to 300 pulses due to shock-induced lattice expansion, which introduces lattice disorder and disrupts atomic order.[57] This disorder increases atomic separation, reducing orbital overlap and raising the energy required for electron transitions between the valence and conduction bands, thus widening the bandgap. Additionally, distortions affect electronic states, contributing to the bandgap increase. The lattice expansion and disorder combination yield a larger bandgap.[58] Shock waves may also cause lattice contraction, which increases orbital overlap in the crystal lattice. This shifts the energy bands closer to the Fermi energy levels, narrowing the gap between conduction and valence bands.

Consequently, this effect reduced ZnTe's bandgap. The inverse relationship between band gap and crystallite size arises from the surface-to-volume ratio, which influences surface atoms and electronic states. Additionally, strain variations in smaller crystallites can alter electronic states, affecting the band gap. The corresponding variation plot is given in Fig. 12(a). It shows that due to the reversible phase transition, ZnTe is capable of tuneable band gap at shock-loading conditions, therefore the material is suggested for photodetector, as a window layer in solar cells and opto-electronic devices under extreme conditions.[59–61]

Photoluminescence spectrum

To explore ZnTe's optical behavior under shock conditions, the photoluminescence spectrum was measured with an excitation wavelength of 325 nm. This experiment reveals that the photoluminescence spectrum of ZnTe exhibits a symmetric and narrow peak at an emission wavelength of 551 nm, consistent with literature reports on ZnTe's characteristic yellow-green emission,[62,63] shown in Fig. 13(a). Also, Fig. 13(b) shows

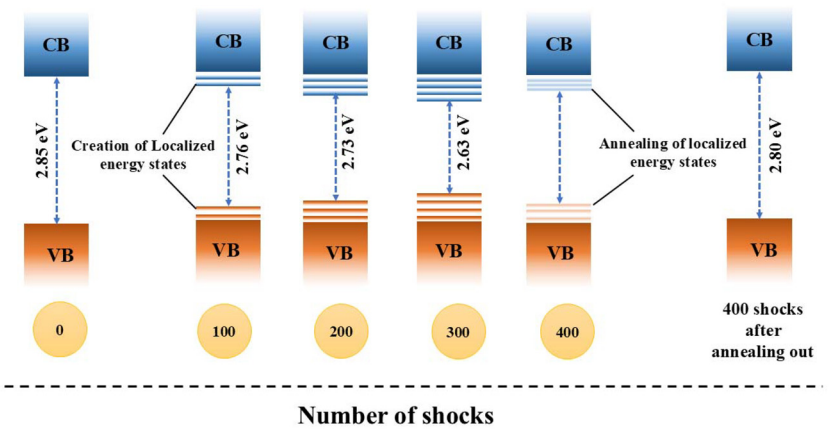

Fig. 11 Energy level diagram of shock-untreated and treated ZnTe.

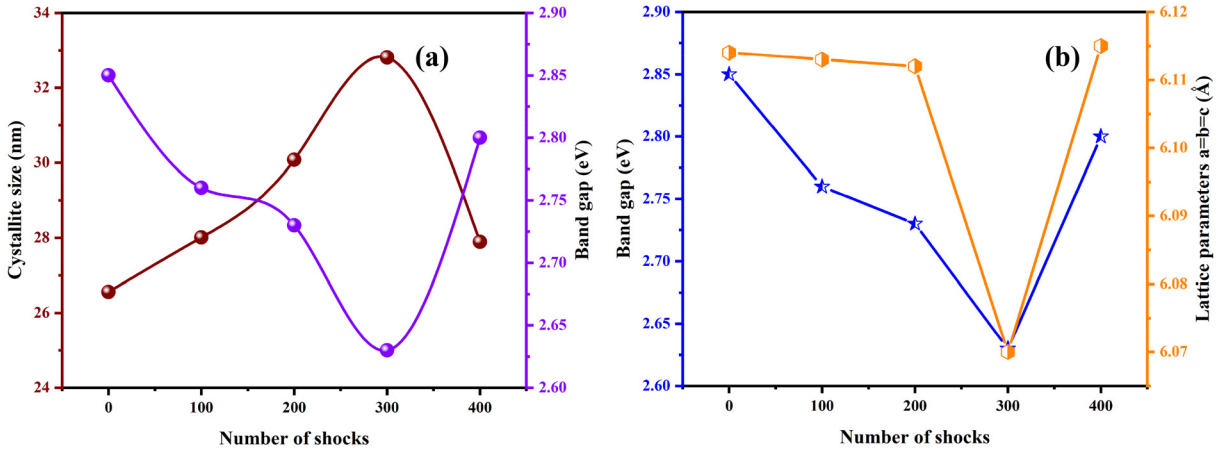

Fig. 12 Variation plots against the number of shock pulses (a) Band gap *vs.* crystallite size. (b) Band gap *vs.* Lattice parameters.

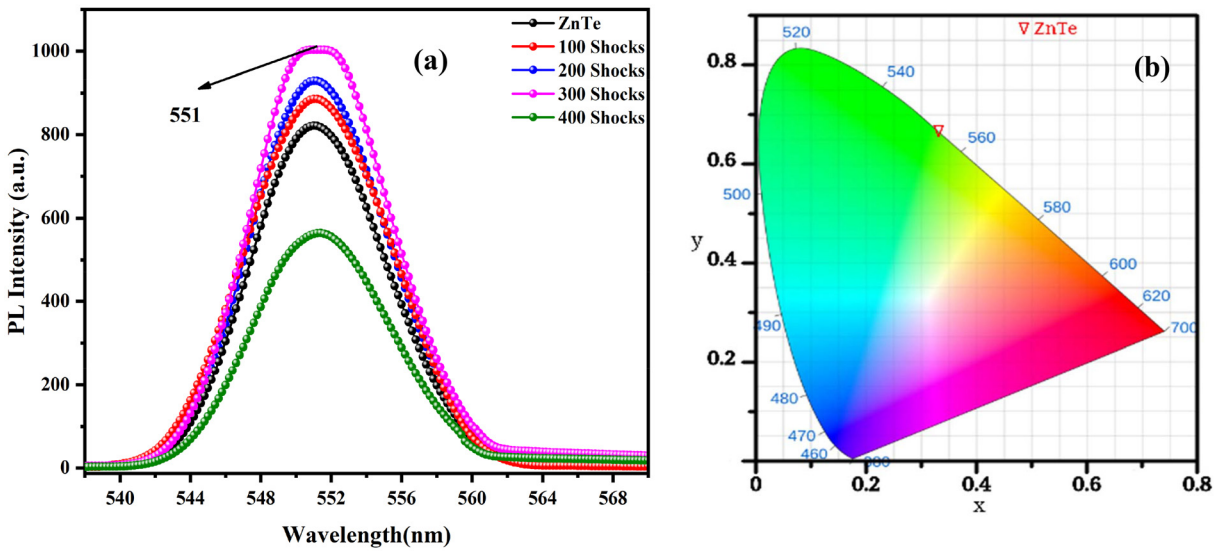

Fig. 13 (a) Photoluminescence Spectra of shock-untreated and treated ZnTe. (b) Chromaticity diagram of shock-untreated ZnTe.

the chromaticity diagram of unshocked ZnTe, the color of the sample ZnTe is graphically represented in a two-dimensional CIE x–y plot. The CIE coordinates are obtained at x = 0.331, and y = 0.664, which is indicated in the red color symbol. This shows that the obtained emission spectrum emits color near to the green-yellow region. Therefore, from the obtained emission colour it is confirmed that the spectrum is correctly correlated with the literature. Compared to the unshocked sample, the emission intensity at 551 nm first exhibits a noticeable increase following 100 shocks. This implies that the shock energy might slightly alter the lattice, perhaps resulting in shallow defects or small lattice strains that promote radiative recombination. These modifications may serve as an effective for photon emission, increasing the intensity of photoluminescence. The intensity increases further when 200 shocks are reached. This ongoing improvement might indicate further improvement in the decrease of the material's defect distribution or improved crystallinity. By decreasing pathways for non-radiative recombination, shock pulses at this level may be assisting the ZnTe lattice in compacting or reorienting slightly, which could enhance photon emission.

However, interestingly, the PL intensity at 300 shocks reached its maximum, suggesting that the sample undergoes significant structural changes that promote maximum radiative recombination. This implies that the shock treatment at this level may result in a new structure that optimally balances defects, enhancing luminescence while minimizing non-radiative pathways. The combination of structural reorganization and defect creation appears to favor conditions that boost radiative efficiency. By opening up previously blocked or unobstructed emission routes, this defect-healing process may increase the material's radiative output.[64] Compared to 300 shocks, the PL intensity decreases at 400 shocks, this decrease might indicate the emergence of non-radiative recombination centers, which

could be brought on by more serious lattice flaws that start to block the earlier observed enhanced emission. This decline raises the possibility that ZnTe is approaching a point at which the shock energy causes structural alterations, most likely through microstructure disruption or the introduction of defect states that non-radiatively trap energy. This pattern of an initial rise, a subsequent fall, and a subsequent strong rise in PL intensity provides information about ZnTe's shock response. According to this, shock treatment can enhance optical characteristics and refine the lattice up to a certain point.

The variation in PL intensity in shock-wave-exposed materials is mainly caused by the shock wave's capacity to increase molecular interactions: when a material undergoes a shock wave exposure, the abrupt changes in temperature and pressure can change the electronic states in the crystal structure, which can change the radiative recombination processes, resulting in either an increase or decrease in PL intensity, depending on the particular changes in the electronic band structure and the local bonding environment.[65]

Moreover, the material's crystallinity is frequently associated with an increase in PL intensity. Less structural flaws are typically associated with high crystallinity, which lowers the number of non-radiative recombination sites that can scatter or trap charge carriers. Larger crystallites generally have lower defect densities and less strain, making them more favorable for radiative recombination. An improved PL response results from more efficient radiative recombination of electron–hole pairs made possible by this reduction in lattice strain.[66,67]

Thus, the correlation between PL intensity and crystallite size is twofold: as crystallite size grows, the density of dislocations and lattice defects reduces, leading to less defect-related scattering and simpler electron–hole recombination routes. Through the reduction of paths that drain energy without emitting light, this structural modification makes the crystal lattice more favourable for high-intensity luminescent emissions. Because the reduction in defect density and lattice strain in larger crystallites minimizes non-radiative pathways, the radiative recombination of electrons and holes, which generates light, is more efficient, leading to an increase in observed PL intensity.[67] According to XRD examination, for 100, 200, and 400 shock pulses, the crystallite size of ZnTe grew as the PL intensity increased. At 300 shock pulses, on the other hand, the crystallite size and PL intensity both shrank. The plot of changes in crystal lite size and PL intensity as a function of shock pulse count is displayed in Fig. 14.

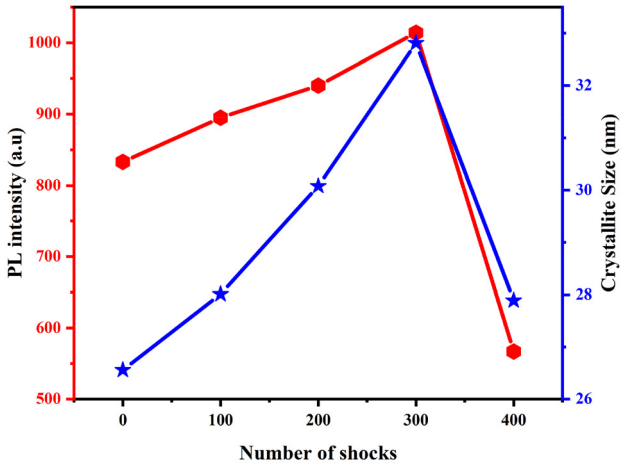

Fig. 14 PL intensity *vs.* crystallite size of ZnTe against the number of shock pulses.

Morphology analysis

The shock wave untreated and treated ZnTe morphology was analyzed with a resolution of 3 nm shown in Fig. 15. The shock untreated sample shows an irregular morphology. The particles are larger, with a rough and flaky appearance, indicating that the material's structure is less compact. This state reflects the material's original condition, where particles tend to form loose aggregates or clusters. After exposure to 100 shock pulses, the particles start to break apart, leading to a reduction in the overall particle size. The agglomeration observed in the shock untreated sample is less prominent here, suggesting that the shock waves have disrupted the inter-particle connections, causing initial fragmentation. The surfaces of the particles appear somewhat smoother, indicating the impact of shock energy in modifying the surface roughness. At 200 shocks the particles exhibit a further decrease in size and appear more uniformly distributed compared to the unshocked state. The smoother surfaces and reduced particle size suggest a combination of fragmentation and compaction, where shock waves have broken down larger particles while simultaneously compressing the smaller fragments. The structure seems more refined, possibly enhancing material density.

With the application of 300 shock pulses, the material undergoes significant refinement, with shock waves inducing both structural and morphological changes. The particles exhibit a noticeable transition in shape, evolving into a more uniform, plate-like structure. The intense pressure and temperature fluctuations caused by the shock waves promote the breakup of larger, irregularly shaped particles, leading to the formation of smaller, more compact shapes. Shock waves induce rapid compression and shear forces, which contribute to particles breaking, and reduction, likely by triggering recrystallization or densification processes. These effects are further supported by the observed increase in homogeneity, indicating that repeated shock exposure continues to influence the material, refining its structure through a combination of fragmentation, compaction, and reshaping. The change in morphology, particularly the development of plate-like features, suggests a phase transformation, where the shock-induced conditions alter the crystal lattice or bond strengths. The reduction in agglomeration and appearance of well-defined particles further suggest that the shock waves not only refine the particle size but also impact the phase and crystallinity of the material, promoting a more ordered structure.

The sample subjected to 400 shocks demonstrates that the structure has undergone further transformation. There are more rugged surfaces and smaller, fragmented particles, indicating

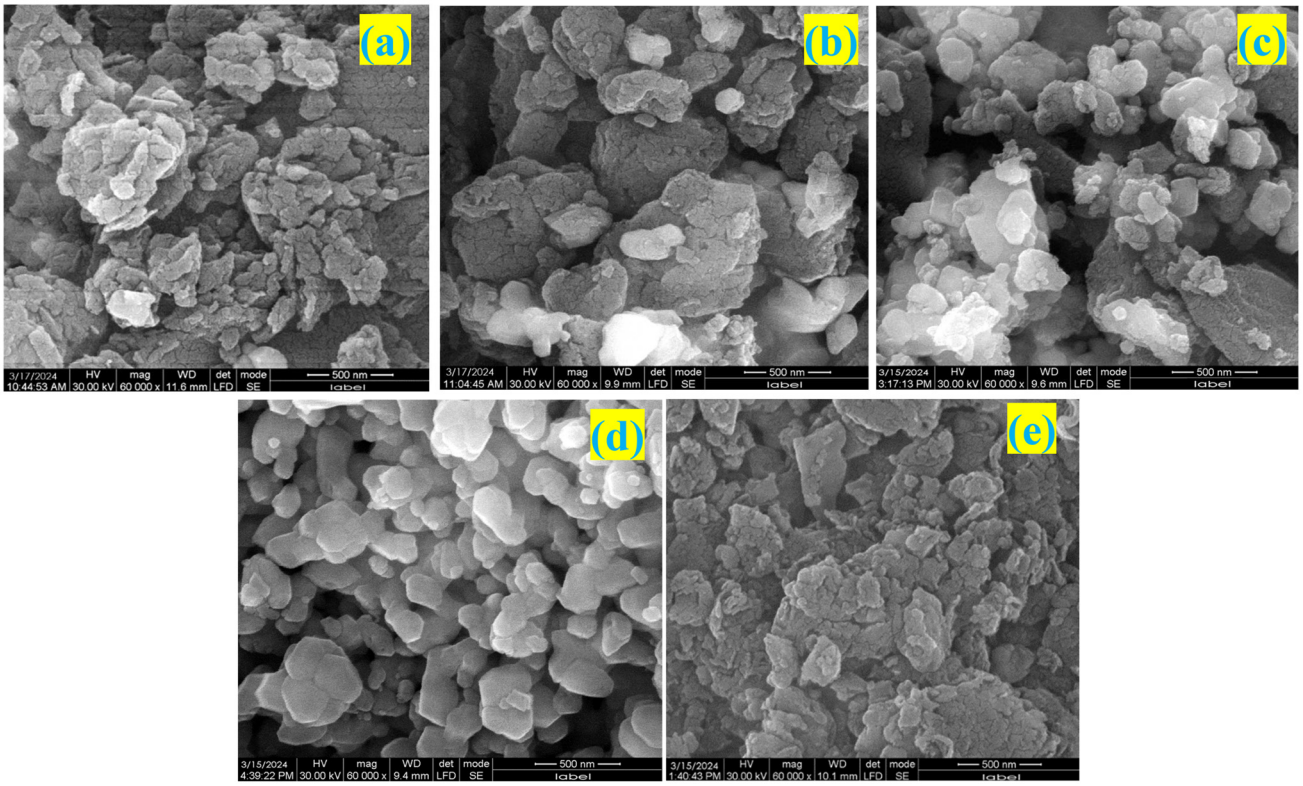

Fig. 15 SEM Images of shock-untreated and treated ZnTe (a) shock untreated ZnTe (b) 100 shocks (c) 200 shocks (d) 300 shocks (e) 400 shocks.

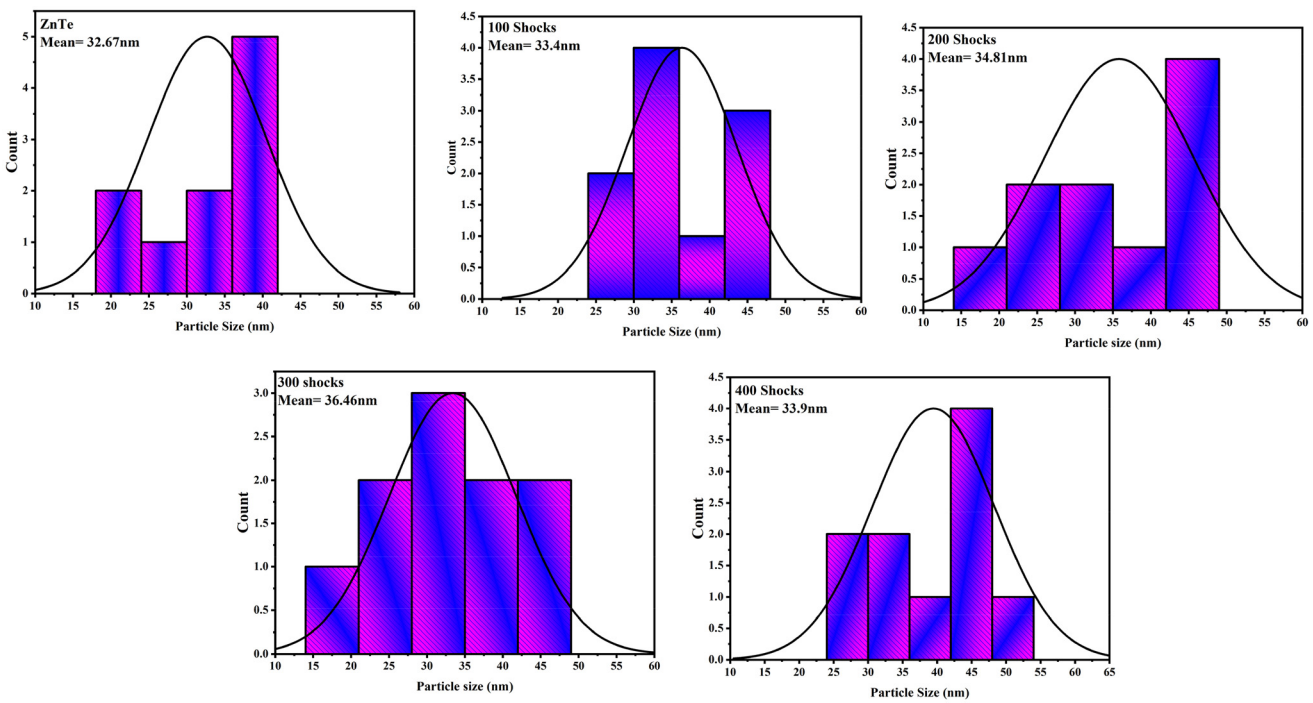

Fig. 16 Average particle size distribution of shock-untreated and treated ZnTe.

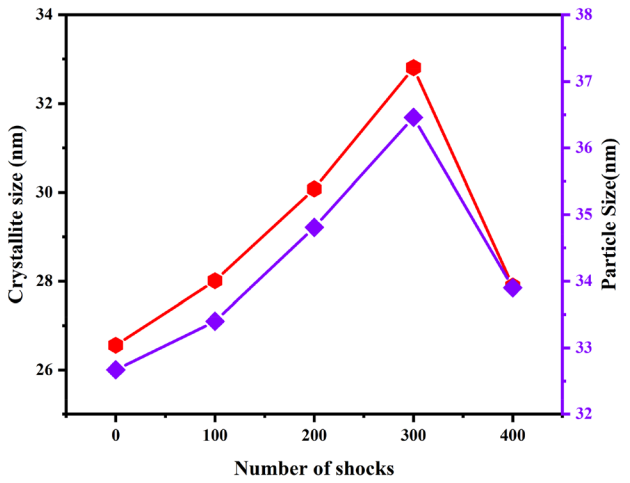

Fig. 17 Particle size *vs.* crystallite size of ZnTe against the number of shock pulses.

significant structural breakdown which resembles the control sample. The shock pulses have likely caused micro-fracturing, leading to fragmentation and increased surface roughness. The material shows progressive densification, particle fusion, reorientation, and eventual fragmentation, which could indicate that the material is undergoing mechanical and possibly phase transformations due to the repeated shock impact. Overall, the sequence of SEM images highlights the progressive transformation of the material's microstructure under the influence of increasing shock. This suggests that shock wave treatment can be an effective method for tailoring the morphology of materials, since the high temperature of the shock waves causes plastic deformation, also because of dynamic recrystallization occur in the sample during the application of shock waves.[68]

Using the ImageJ software the average particle size of the shock untreated and treated ZnTe was calculated. The average particle size was 32.67 nm for the shock untreated sample, at 100 shocks- 33.4 nm, 200 shocks- 34.8 nm, 300 shocks- 36.46 nm, and 400 shocks- 33.90 nm, corresponding average particle size distribution is shown in Fig. 16. The change in particle size is due to shock induces dynamic recrystallization within in the material, cause breakage and fusion of grain boundaries.[69,70] The particle and crystallite size are interrelated to one another, so changes in particle and crystallite size are bound to happen in the same.[71] Fig. 17 shows the directly proportional relation of crystallite and particle size against the impact of shock waves.

Conclusion

In conclusion, this work examined how shock wave exposure affected the optical, morphological, and structural characteristics of zinc telluride (ZnTe). A reversible phase transition between cubic ($F\text{-}\bar{4}3m$) and cubic ($Fm\bar{3}m$) structures was verified by X-ray diffraction analysis; it started at 300 shock pulses and ended at 400 pulses, returning to the initial phase. The phase reversibility and structural robustness of ZnTe under dynamic shock conditions were confirmed by Raman spectroscopy, which revealed comparable peak fluctuations in intensity, disappearance of peak and position. With a noticeable change in absorption spectrum has increase in band gap from 2.85 eV to 2.63 eV after 300 pulses and increase to 2.80 eV after 400 pulses, optical examination demonstrated a tuneable band gap, indicating improved photon absorption capabilities at particular shock levels. The photoluminescence spectrum showed heightened emission intensity under 300 shock pulses, indicating the formation of optical centers associated with the phase change. Scanning electron microscopic analysis revealed a transformation in morphology, evolving from irregular forms to plate-like structures with some irregular shapes at 300 pulses, which reverted at 400 pulses, demonstrating reversible morphological adaptation. These findings confirm ZnTe's robust stability and the ability of shock waves to modulate its structural and optical properties without permanent alterations to the crystal framework. The reversibility of phase transitions and tuneable band gap makes ZnTe a compelling candidate for optoelectronic applications, such as sensors and photodetectors, that demand resilience under extreme mechanical conditions. This adaptability highlights its potential in situations where materials are subjected to repeated mechanical stress, establishing ZnTe as a promising material for long-lasting, high-performance optoelectronics.

Author contributions

S. Oviya – contributed to investigation, data analysis and writing the original draft. F. Irine Maria Bincy – contributed to data analysis. Raju Suresh Kumar and P. Kannappan contributed to the formal analysis, and Ikhyun Kim – contributed to the formal analysis. S. A. Martin Britto Dhas – contributed to conceptualization, writing and editing.

Data availability

The data in this manuscript can be obtained from the corresponding author.

Conflicts of interest

The authors declare that they have no conflicts of interest regarding the publication of this paper.

Acknowledgements

The authors would like to thank the Abraham Panampara Research Fellowship (APRF). The authors thank the Management of Sacred Heart College for the financial support through Fr. Carreno Research Grant (SHC/Fr. Carreno

Research Grant/2024/03). This research was supported by the Brain Pool program funded by the Ministry of Science and ICT (MSIT) through the National Research Foundation of Korea (RS-2023-00219593) and through the NRF funded by the MSIT Grant No. 2022R1C1C1006414. Also, this project was supported by the Researchers Supporting Project Number (RSP2025R142), King Saud University, Riyadh, Saudi Arabia.

References

1 K. Ichiyanagi, S. Takagi, N. Kawai, R. Fukaya, S. Nozawa, K. G. Nakamura, K. D. Liss, M. Kimura and S. I. Adachi, Microstructural deformation process of shock-compressed polycrystalline aluminium, *Sci. Rep.*, 2019, **9**, 7604.
2 A. Sivakumar, S. Suresh, J. Anto Pradeep, S. Balachandar and S. A. Martin Britto Dhas, Effect of shock waves on dielectric properties of KDP crystal, *J. Electron. Mater.*, 2018, **47**, 4831–4839.
3 G. I. Kanel, V. E. Fortov and S. V. Razorenov, Shock waves in condensed-state physics, *Phys.-Usp.*, 2007, **50**, 771–791.
4 A. Sivakumar, A. Saranraj, S. Sahaya Jude Dhas, M. Jose and S. A. Martin Britto Dhas, Shock wave-induced defect engineering for investigation on optical properties of triglycine sulphate crystal, *Opt. Eng.*, 2019, **58**, 077104.
5 A. Rita, A. Sivakumar and S. A. Martin Britto Dhas, Influence of shock waves on structural and morphological properties of copper oxide NPs for aerospace applications, *J. Nanostruct. Chem.*, 2019, **9**, 225–230.
6 N. Zhao, M. Sugiyama and T. Ruggeri, Phase transition induced by a shock wave in hard-sphere and hard-disk systems, *J. Chem. Phys.*, 2008, **129**, 054506.
7 S. J. Wang, M. L. Sui, Y. T. Chen, Q. H. Lu, E. Ma, X. Y. Pei, Q. Z. Li and H. B. Hu, Microstructural fingerprints of phase transitions in shock-loaded iron, *Sci. Rep.*, 2013, **3**, 1086.
8 S. Kalaiarasi, A. Sivakumar, S. A. Martin Britto Dhas and M. Jose, Shock wave induced anatase to rutile TiO_2 phase transition using pressure driven shock tube, *Mater. Lett.*, 2018, **219**, 72–75.
9 A. Sivakumar, S. Reena Devi, S. Sahaya Jude Dhas, R. M. Kumar, K. K. Bharathi and S. A. Martin Britto Dhas, Switchable phase transformation (Orthorhombic - Hexagonal) of potassium sulfate single crystal at ambient temperature by shock waves, *Cryst. Growth Des.*, 2020, **20**, 7111–7119.
10 A. Sivakumar, A. Rita, S. Sahaya Jude Dhas, K. P. J. Reddy, R. Suresh Kumar, A. I. Almansour, S. Chakraborty, K. Moovendaran, J. Sridhar and S. A. Martin Britto Dhas, Dynamic shock wave driven simultaneous crystallographic and molecular switching between α-Fe_2O_3 and Fe_3O_4 nanoparticles-a new finding, *Dalton Trans.*, 2022, **51**, 9159–9166.
11 F. Irine Maria Bincy, S. Oviya, R. Suresh Kumar, P. Kanappan, I. Kim and S. A. Martin Britto Dhas, Acoustic shock wave-induced reversible phase transition (rhombohedral to hexagonal) of bismuth telluride, *J. Mater. Sci.*, 2024, **59**, 7044–7059.
12 V. Mowlika, A. Sivakumar, S. A. Martin Britto Dhas, C. S. Naveen, A. R. Phani and R. Robert, Shock wave induced switchable magnetic phase transition behaviour of $ZnFe_2O_4$ ferrite nanoparticles, *J. Nanostruct. Chem.*, 2020, **10**, 203–209.
13 A. Rita, A. Sivakumar, S. Sahaya Jude Dhas and S. A. Martin Britto Dhas, Reversible magnetic phase transitions of MnO_2 nanorods by shock wave recovery experiments, *J. Mater. Sci.:Mater. Electron.*, 2020, **31**, 20360–20367.
14 A. Sivakumar, S. Soundarya, S. Sahaya Jude Dhas, K. K. Bharathi and S. A. Martin Britto Dhas, Shock wave driven solid-state phase transformation of Co_3O_4 to CoO nanoparticles, *J. Phys. Chem. C*, 2020, **124**, 10755–10763.
15 K. S. Zh, P. Ravindran, A. Kjekshus, H. Fjellvag and B. G. Svensson, Electronic structure and optical properties of Zn X (X = O, S, Se, Te): A density functional study, *Phys. Rev. B:Condens. Matter Mater. Phys.*, 2007, **75**(15), 155104.
16 K. Sato, M. Hanafusa, A. Noda, A. Arakawa, M. Uchida, T. Asahi and O. Oda, ZnTe pure green light-emitting diodes fabricated by thermal diffusion, *J. Cryst. Growth*, 2000, **214**, 1080–1084.
17 S. Chen, Y. Runsheng, L. Song, R. Zhang, X. Cao, B. Wang and P. Zhang, Effect of low-temperature vulcanization time on the structure and optical properties of ZnS thin films, *Appl. Surf. Sci.*, 2019, **498**, 143876.
18 H. H. Gullu, O. Bayrakl, D. E. Yildiz and M. Parlak, Study on the electrical properties of ZnSe/Si heterojunction diode, *J. Mater. Sci.: Mater. Electron.*, 2017, **28**, 17806–17815.
19 H. Mukul and J. Datta, Optimal blending of PbSe and CdSe in polycrystalline PbCdSe nanocomposite film: improved carrier multiplication and enhanced photoconversion efficiency, *ACS Appl. Mater. Interfaces*, 2019, **11**(43), 40393–40405.
20 T. Chen, X. Wang, P. Han, W. Sun, S. Feng, J. Ye, Y. Xu and Y. Zhang, First-and second-order photon-phonon interactions and optical parameters of ZnTe crystal: a broadband terahertz time-domain spectroscopy study, *J. Phys. D: Appl. Phys.*, 2019, **52**(45), 455101.
21 O. I. Olusola, M. L. Madugu, N. A. Abdul-Manaf and I. M. Dharmadasa, Growth and characterization of n-and p-type ZnTe thin films for applications in electronic devices, *Curr. Appl. Phys.*, 2016, **16**(2), 120–130.
22 W. S. Kuhn, A. Lusson, B. Qu Hen, C. Grattepain, H. Dumont, O. Gorochov, S. Bauer, K. Wolf, M. Worz, T. Reisinger and A. Rosenauer, The metal-organic vapour phase epitaxy of ZnTe: III. Correlation of growth and layer properties, *Prog. Cryst. Growth Charact. Mater.*, 1995, **31**(1–2), 119–177.
23 S. V. Ovsyannikov and V. V. Shchennikov, Thermoelectric properties of the trigonal and orthorhombic modifications of zinc telluride, *J. Exp. Theor. Phys. Lett.*, 2004, **80**, 35–38.
24 A. Ohtani, M. Motobayashi and A. Onodera, Polymorphism of ZnTe at elevated pressure, *Phys. Lett. A*, 1980, **75**(5), 435–437.

25 R. J. Nelmes, Crystal structure of ZnTe III at 16 GPa, *Phys. Rev. Lett.*, 1994, **73**(13), 1805.
26 M. I. McMahon, R. J. Nelmes, N. G. Wright and D. R. Allan, In Proc. of the Joint AIEAPTIAPS Topical Conf. on High-Pressure Science and Technology, ed. Schmidt S C, Shoner J W, Samara G A and Ross M, 1995, *J. Phys. Chem. Solids*, 1994, **56**, 545.
27 R. J. Nelmes, Structural studies of II-VI semiconductors at high pressure, *J. Phys. Chem. Solids*, 1995, **56**(3–4), 545–549.
28 Y. Zhuang, L. Dai, H. Li, H. Hu, K. Liu, L. Yang, C. Pu and M. Hong, Pressure-induced reversible metallization and phase transition in Zinc Telluride, *Mod. Phys. Lett. B*, 2018, **32**(28), 1850342.
29 C. Pu, L. Dai, H. Li, H. Hu, K. Liu, L. Yang and M. Hong, Pressure-induced phase transitions of ZnSe under different pressure environments, *AIP Adv.*, 2019, **9**(025004), 1–7.
30 K. Kusaba and D. J. Weidner, Structure of high pressure phase I in ZnTe, *AIP Conference Proceedings*, Vol. 309, No. 1, pp. 553–556.
31 B. Bahloul, B. Deghfel, L. Amirouche, A. Bentabet, Y. Bouhadda and S. Bounab, Nouredine, Fenineche. Ab initio study of the structural, electronic and optical properties of ZnTe compound, *AIP Conf. Proc.*, 2015, **1653**, 020019.
32 J. Minglin, F. He, S. Zheng, Y. Xu, Y. Peng, X. Chen and X. Hu, Growth of ZnTe Semiconductor Crystal Via a Te Flux Zone Melting Method and Characterization of Its Properties, *Cryst. Res. Technol.*, 2022, **57**(10), 2100279–2100279.
33 Y. Yin, G. Chen, H. Ye, X. Duan and Y. Zhu, Yelong Wu A novel anion interstitial defect structure in zinc-blende materials: A first-principles study, *EPL*, 2016, **114**(3), 36001.
34 H. Bilz and W. Kress, *Zinc-Blende Structure Crystals*, Springer, Berlin, Heidelberg, 1979, pp. 101–116.
35 A. Sivakumar, L. Dai, S. Sahaya Jude Dhas, R. Sures Kumar, A. I. Almansour and S. A. Martin Britto Dhas, tuning of lower to higher crystalline nature of β-L-Glutamic acid by shock waves, *J. Mol. Struct.*, 2023, **1288**, 135788–135795.
36 K. Ichiyanagi and K. G. Nakamura, Structural dynamics of materials under sock compression investigated with synchrotron radiation, *Metals*, 2016, **6**(1), 17.
37 B. Nasiri-Tabrizi, Thermal treatment effect on structural features of mech nano-synthesized fluorapatite-titania nanocomposite: a comparative study, *J. Adv. Ceram.*, 2014, **3**(1), 31–42.
38 C. O. Ei-Eromosele, B. I. Ita and E. E. J. Iweala, Low-temperature combustion synthesis of cobalt magnesium ferrite magnetic nanoparticles effects of fuel-to-oxidizer ratio and sintering temperature, *J. Sol-Gel Sci. Technol.*, 2015, **76**(2), 298–308.
39 B. Azhdar, Influence of fuel-to-oxidizer ratio, potential of hydrogen and annealing temperature on the structural and optical properties of nanocrystalline MgO powders synthesized by the hydrothermal method, *J. Exp. Nanosci.*, 2023, **18**(1), 2276278–2276299.
40 A. Rita, A. Sivakumar and S. A. Martin Britto Dhas, Influence of shock waves on structural and morphological properties of copper oxide NPs for aerospace applications, *J. Nanostruct. Chem.*, 2019, **9**, 225–230.
41 M. Shobana and S. R. Meher, Experimental and ab initio study of the structural, electronic, and vibrational properties of ZnTe, *J. Alloys Compd.*, 2018, **762**, 260–271.
42 H. H. Gullu, O. Bayrakli Surucu, M. Isik, M. Terlemezoglu and M. Parlak, Material and Si-based diode analyses of sputtered ZnTe thin films, *J. Mater. Sci.: Mater. Electron.*, 2020, **31**, 11390–11397.
43 K. Ersching, C. E. M. Campos, J. C. de Lima, T. A. Grandi, S. M. Souza, D. L. da Silva and P. S. Pizani, X-ray diffraction, Raman, and photoacoustic studies of ZnTe nanocrystals, *J. Appl. Phys.*, 2009, **105**, 123532.
44 H. Saqib, S. Rahman, D. Errandonea, R. A. Susilo, A. Jorge-Montero, P. Rodriguez-Hernndez and A. Munoz, Giant conductivity enhancement: Pressure-induced semiconductor-metal phase transition in $Cd_{0.90}Zn_{0.1}Te$, *Phys. Rev. B*, 2019, **99**, 094109.
45 E. Mosquera, Structure and photoluminescence from naturally dispersed ZnTe nanoparticles, *Mater. Express*, 2019, **9**, 173–178.
46 A. Bera, D. V. S. Muthu and A. K. Sood, Enhanced Raman and photoluminescence response in monolayer MoS_2 due to laser healing of defects, *J. Raman Spectrosc.*, 2018, **49**(1), 100–105.
47 M. Okuno, B. Reynard, Y. Shimada, Y. Syono and C. Willaime, A Raman spectroscopic study of shock-wave densification of vitreous silica, *Phys. Chem. Miner.*, 1999, **26**, 304–311.
48 S. S. Kale, R. S. Mane, H. M. Pathan, A. V. Shaikh, O. S. Joo and S. H. Han, Preparation and characterization of ZnTe thin films by SILAR method, *Appl. Surf. Sci.*, 2007, **253**, 4335–4337.
49 H. Singh, T. Singh and J. Sharma, Review on optical, structural and electrical properties of ZnTe thin films: effect of deposition techniques, annealing and doping, *ISSS J. Micro Smart Syst.*, 2018, **7**(2), 123–143.
50 R. Sreekumar, R. Jayakrishnan, C. Sudha Kartha, K. P. Vijayakumar and S. A. Khan, Enhancement of band gap and photoconductivity in gamma indium selenide due to swift heavy ion irradiation, *J. Appl. Phys.*, 2008, **103**, 1–9.
51 S. Oviya, F. Irine Maria Bincy, S. Arumugam, K. Kamala Bharathi, R. Suresh Kumar, P. Kannappan, I. Kim and S. A. Martin Britto Dhas, Acoustic shock wave-induced phase transition in indium selenide: tuning band gap energy for solar cell applications, *CrystEngComm*, 2024, **26**, 2498–2509.
52 S. Oviya, F. Irine Maria Bincy, R. Suresh Kumar, P. Kannappan, I. Kim and S. A. Martin Britto Dhas, Tuning the Band Gap of Bismuth Sulfide via Acoustic Shock Waves to Harness the Full Visible Spectrum for Enhanced Solar Cell Applications, *Mater. Chem. Phys.*, 2024, 130287.
53 F. Irine Maria Bincy, S. Oviya, R. Suresh Kumar, P. Kannappan, S. Arumugam, I. Kim and S. A. Martin

Britto Dhas, Investigation of bismuth selenide's structural stability and tunable bandgap under exposure to acoustic shock waves for solar cell and aerospace applications, *Mech. Adv. Mater. Struct.*, 2024, 1–15.

54 Y. Kanemitsu, Y. Isida, I. Nakada and H. Kuroda, Anomalous surface transformations in crystalline silicon induced by subpicosecond laser pulses, *Appl. Phys. Lett.*, 1986, **48**(3), 209–211.

55 M. Riaz, B. Ali, S. Mansoor Ali, M. Ijaz Kan, M. Sana Ulla Sahar, M. Shahid and M. Alam, Stress-induced transformation on the cubic perovskite $RbTaO_3$ for high-temperature applications: a DFT approac, *J. Comput. Electron.*, 2024, **23**(3), 483–497.

56 M. Sarma, S. Murugavel, D. Kumar Sukla and F. M. F. de Groot, Reversal in the lattice contraction of α-Fe_2O_3 nanoparticles, *J. Phys. Chem. C*, 2018, **122**(17), 9292–9301.

57 M. S. Scneider, B. Kad, D. H. Kalantar, B. A. Remington, E. Kenik, H. Jarmakani and M. A. Meyers, Laser shock compression of copper and copper-aluminum alloys, *Int. J. Impact Eng.*, 2005, **32**(1–4), 473–507.

58 N. Katun, E. G. Rini, P. Sirage, P. Rajput, S. N. Ja and S. Sen, Effect of lattice distortion on bandgap decrement due to vanadium substitution in TiO_2 nanoparticles, *Mater. Sci. Semicond. Process.*, 2016, **50**, 7–13.

59 A. A. Ibrahim, N. Z. El-Sayed, M. A. Kaid and A. Ashour, Structural and electrical properties of evaporated ZnTe thin films, *Vacuum*, 2004, **75**, 189–194.

60 A. A. Ibrahim, DC electrical conduction of zinc telluride thin films, *Vacuum*, 2006, **81**, 527–530.

61 K. Yoshino, A. Memon, M. Yoneta, K. Ohmori, H. Sato and M. Ohishi, Optical characterization of the ZnTe pure-green LED, *Phys. Status Solidi B*, 2002, **229**, 977–980.

62 B. Wan, C. Hu, B. Feng, J. Xu, Y. Zhang and Y. Tian, Optical properties of ZnTe nanorods synthesized via a facile low-temperature solvothermal route, *Mater. Sci. Eng., B*, 2010, **171**, 11–15.

63 X. Xing, D. Wang, Z. Chen, B. Zheng, B. Li and D. Wu, ZnTe quantum dots as fluorescence sensors for the detection of iron ions, *J. Mater. Sci.: Mater. Electron.*, 2018, **29**, 14192–14199.

64 A. Schwarz, H. Alon-Yehezkel and A. Levi, Thiol-based defect healing of WSe_2 and WS_2, *npj 2D Mater. Appl.*, 2023, **7**(59), 1–9.

65 J. Guan, C. Zhang, D. Gao, X. Tang, X. Dong, X. Lin, Y. Wang, X. Wang, L. Wang, H. Hwi Lee, J. Xu, H. Zheng, K. Li and H. Mao, Drastic photoluminescence modulation of an organic molecular crystal with high pressure, *Mater. Chem. Front.*, 2019, **3**, 1510–1517.

66 K. Amarsingh Bhabu, J. Theerthagiri, J. Madhavan, T. Balu, G. Muralidharan and T. R. Rajasekaran, Enhanced electrochemical behavior of ceria-based zirconia electrolytes for intermediate temperature solid oxide fuel cell applications, *J. Mater. Sci.:Mater. Electron.*, 2016, **27**, 10980–10992.

67 C. Mrabet, M. Ben Amor, A. Boukhachem, M. Amlouk and T. Manoubi, Physical properties of La-doped NiO sprayed thin films for optoelectronic and sensor applications, *Ceram. Int.*, 2016, **42**, 5963–5978.

68 Y. Wang, G. Wang, N. Xiang and Y. Aheng, Microstructural evolution and high temperature deformation mechanism of 4Cr5MoSiV1Ti steel, *J. Mater. Res. Technol.*, 2023, **24**, 8856–8865.

69 A. Rita, A. Sivakumar, S. Sahaya Jude Dhas and S. A. Martin Britto Dhas, Structural, optical, and magnetic properties of silver oxide (AgO) nanoparticles at shocked conditions, *J. Nanostruct. Chem.*, 2020, **10**, 309–316.

70 T. Sekine, N. Ozaki, K. Miyanishi, Y. Asaumi, T. Kimura, B. Albertazzi, Y. Sato, Y. Sakawa, T. Sano, S. Sugita, T. Matsui and R. Kodama, Shock compression response of forsterite above 250 GPa, *Sci. Adv.*, 2016, **2**, 16001573.

71 M. I. Amal, J. T. Wibowo, L. Nuraini, G. Senopati, M. Y. Hasbi and G. Priyotomo, Antibacterial activity of copper oxide nanoparticles prepared by mechanical milling, *Mater. Sci. Eng.*, 2019, **578**, 012039–012047.

